Available online at www.sciencedirect.com
SCIENCE DIRECT®
ELSEVIER
Mechanics of Materials 35 (2003) 481–509
MECHANICS OF MATERIALS
www.elsevier.com/locate/mechmat

Modeling dynamic crack propagation in fiber reinforced composites including frictional effects ☆

S.K. Dwivedi [1], H.D. Espinosa *

Department of Mechanical Engineering, Northwestern University, 2145 Sheridan Road, Evanston, IL 60208-3111, USA

Received 17 September 2001; received in revised form 29 April 2002

Abstract

Dynamic crack propagation in a unidirectional carbon/epoxy composite is studied through finite element analyses of asymmetric impact (shear loading) of a rod against a rectangular plate. A finite deformation anisotropic visco-plastic model is used to describe the constitutive response of the composite. Crack propagation is simulated by embedding zero thickness interface element along the crack path. An irreversible mixed-mode cohesive law is used to describe the evolution of interface tractions as a function of displacement jumps. Contact and friction behind the crack tip are accounted for in the simulations. The failure of the first interface element at the pre-notch tip models onset of crack extension. Crack propagation is modeled through consecutive failure of interface elements. The dynamic crack propagation phenomenon is studied in terms of crack initiation time, crack speed, mode I and mode II displacement jumps and tractions associated with the failure of interface elements, effective plastic strain at the crack tip and path independent integral J'. Analyses are carried out at impact velocities of 5, 10, 20, 30 and 40 m/s, assuming the crack wake is frictionless. Moreover, analyses at impact velocities of 30 and 40 m/s are also carried out with a friction coefficient of 0.5, 1, 5 and 10 along the crack surfaces. The analyses show that steady-state intersonic crack propagation in fiber reinforced composite materials occurs when the impact velocity exceeds a given threshold. A steady-state crack speed of 3.9 times the shear wave speed and 83% of the longitudinal wave speed is predicted in the cases in which the impact velocity is above 10 m/s. Detailed discussion is given on the features of sub-sonic and intersonic crack propagation. It is shown that friction effects, behind the crack tip, do not have a significant effect on maximum crack speed; however, they do on characteristics of the shock wave trailing the crack tip. The analyses also show that the contour integral J', computed at contours near the crack tip, is indeed path independent and can serve as a parameter for characterizing intersonic crack propagation.

☆ This article is based on presentations given at the ASME International Congress and Exposition, November 1998, Los Angeles, CA, and an ARO-MURI review meeting. The research here reported was then published in the second author's web page but otherwise remained unpublished. The reader will find the status of the subject, reported analyses and conclusions as given in the original presentations. Since then, several contributions have been made by various research groups. For completeness these contributions are cited and discussed in the context of the reported numerical simulations.

* Corresponding author. Tel.: +1-847-467-5989; fax: +1-847-491-3915.
E-mail address: espinosa@northwestern.edu (H.D. Espinosa).
URL: http://clifton.mech.northwestern.edu/~espinosa.
[1] Currently at Institute of Shock Physics, Washington State University, Pullman, WA 99164-2816, USA.

0167-6636/03/$ - see front matter
PII: S0167-6636(02)00266-1

1. Introduction

Dynamic crack propagation in materials has remained an active area of research for decades. In the past few years, the importance of this area has re-emerged, primarily due to (a) greater emphasis on multi-layered materials in strategic applications, (b) role of dynamic crack propagation in determining the overall response and damage mode of advanced materials, and (c) experimental findings showing that the velocity of a dynamically growing crack can exceed the shear wave speed of the materials. It is this feature that has drawn much attention in recent years.

There have been a number of experimental measurements on initiation and dynamic propagation of cracks along bimaterial interfaces, Tippur and Rosakis (1991), Tippur et al. (1991), Rosakis et al. (1991), Lambros and Rosakis (1995a,b,c), Singh and Shukla (1996), Singh et al. (1997a), and Kumar and Kishore (1998). In these experiments, as shown in Fig. 1, half of the bimaterial specimen is made of a metal, aluminum or steel, and the other half is made of a more compliant material, e.g., PMMA or Homalite. The specimen is asymmetrically impact loaded and the crack propagates dynamically under the influence of intense stress waves. A number of important results have been reported from these experiments. At an impact velocity of less than 5 m/s, the extension and dynamic growth of the crack has been found to occur predominantly in mode I. The maximum crack speed, V_c, is observed to be 80% of the Rayleigh wave speed, C_R, of the more compliant material, i.e., PMMA or Homalite. These crack speeds $V_c < C_s$, where C_s is the shear wave speed of the more compliant material, have been termed subsonic crack speeds. At an impact velocity of more than 20 m/s, crack extension and propagation takes place in predominantly shear or mode II. For these

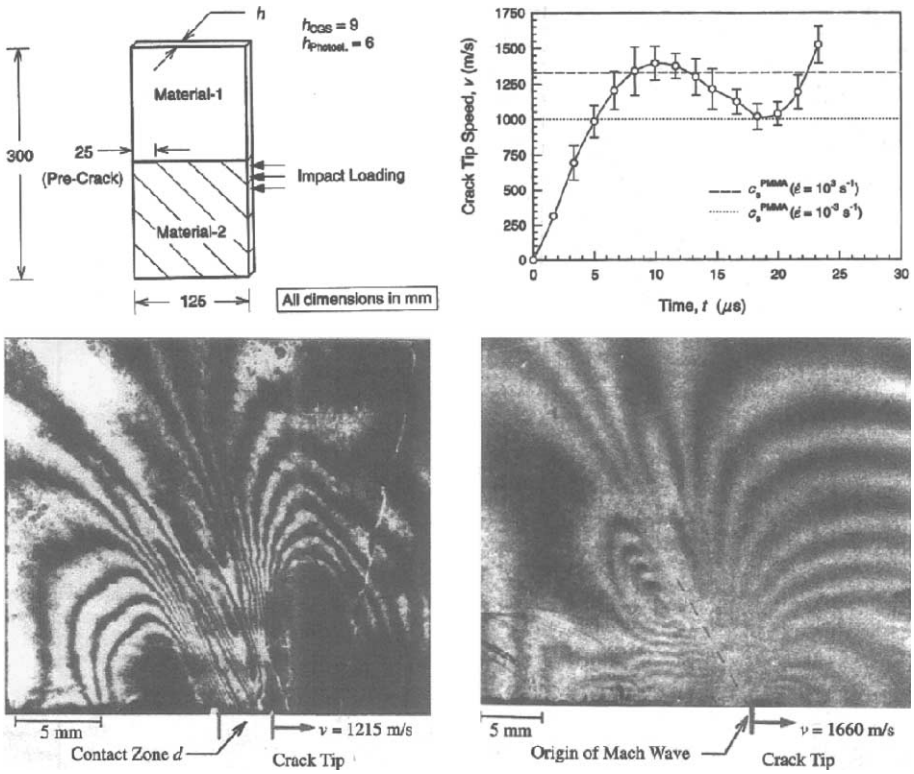

Fig. 1. Schematic of dynamic crack propagation experiment and intersonic crack propagation event reproduced from Singh et al. (1997a).

shear driven cracks, maximum speed of propagation has been found to be as high as $1.5C_s$. These crack speeds $C_s < V_c < C_l$, where C_l is the dilational wave speed of the more compliant material, have been termed intersonic crack speeds.

The intersonic crack propagation phenomenon, along a bimaterial interface, was at first puzzling. In fact, theory predicts that sustained mode I crack propagation in homogeneous materials, at a speed equal to the Rayleigh speed of the material, requires an infinite amount of energy. Other interesting observations were: (i) crack tip acceleration in the intersonic region is reported to be as high as $10^7 g$, where g is the gravitational acceleration; (ii) development of a contact zone and the formation of lines of discontinuity (shock waves) behind intersonically propagating cracks.

Analyses of these experimental records have been carried out using analytical solutions of the two dimensional, singular, elastic crack tip stress fields problem, Rice et al. (1990), Wu (1991), Liu et al. (1993), Liu et al. (1995), Ricci et al. (1997), Singh et al. (1997b), and Kavaturu and Shukla (1998). It has been shown that the ratio between displacement along the crack and a direction normal to it, remains constant behind the dynamically propagating crack. This ratio is less than unity (of the order of 0.3) in the sub-sonic regime exhibiting mode I cracking, whereas it is more than unity (of the order of 3.0) in the intersonic regime exhibiting mode II cracking. Furthermore, the strain energy release rate decreases with the increase in crack speed and approaches zero in the intersonic region. The analyses have also confirmed the existence of a contact zone and formation of a Mach zone behind intersonically propagating cracks.

In spite of the these crucial findings, there are some discrepancies in the experimental characterization of dynamic crack propagation. Experimental studies by Tippur and Rosakis (1991), Tippur et al. (1991), Rosakis et al. (1991), and Lambros and Rosakis (1995a,b,c), did not establish a steady-state intersonic crack propagation. Using a larger width of bimaterial specimen, Singh et al. (1997a) showed that a steady-state intersonic crack speed can be achieved. Similarly, according to Lambros and Rosakis (1995a) and Liu et al. (1995), there exists an unfavorable velocity regime, $C_s < V_c < \sqrt{2}C_s$, in which the crack growth is unstable and the crack quickly accelerates out of this region. In contrast, Singh et al. (1997a) have shown that stable crack growth indeed takes place in this regime. Instead of strain energy release rate reducing monotonously to zero as in Lambros and Rosakis (1995a), Kavaturu and Shukla (1998) have shown that it first increases with crack speed and then, after attaining a maximum, it starts decreasing and approaches zero.

There are two obvious reasons for such discrepancies. First, experimentation with a smaller width of plates, Tippur and Rosakis (1991), Tippur et al. (1991), Rosakis et al. (1991), and Lambros and Rosakis (1995a,b,c), did not allow intersonic crack propagation to reach the steady state due to boundary effects. Second, the crack tip stress field solutions used to derive the above conclusions are based on the assumption that stress fields are elastic, crack front extends infinitely and crack faces are traction-free. In actual experiments, some of these assumptions are not met. Due to stress concentration, the crack tip is always associated with an inelastic regime. The interaction between reflected stress waves and dynamic crack fronts is unavoidable. Furthermore, because of contact behind the crack the intersonically propagating crack wake is not free of traction. Additionally, there are frictional effects in the contact zone which modify the crack tip stress fields and its propagation characteristics. *These observations illustrate the complexity of the problem and the need for detailed numerical studies.*

There have been a number of computational studies on bimaterial interface cracks, Shih and Asaro (1990), Varias et al. (1990a, 1990b), Yang et al. (1991), Nakamura et al. (1995), Xu and Needleman (1995), Xu and Needleman (1996), Siegmund et al. (1997), Kumar and Kishore (1998), and Needleman and Rosakis (1999), to mention a few. However, few analyses have been conducted to study the intersonic crack propagation and the effect of various factors. Nakamura et al. (1995) used the strain energy release rate as the governing criteria for dynamic propagation of cracks and found that the dynamic J' integral approaches zero with the increase in crack velocity. Xu and Needleman (1996), and Needleman

and Rosakis (1999), carried out an extensive parametric study with the help of assumed material properties and obtained intersonic crack speeds and a contact zone behind the propagating crack. However, the interface cohesive elements used by Xu and Needleman (1996), and Needleman and Rosakis (1999), did not include frictional effects after failure and creation of free surfaces. It should be noted that in their model the dynamic J' integral does not decrease with increasing crack speed.

Recently, Rosakis et al. (1999) showed that intersonic shear cracks also occur in homogeneous materials in which a weak plane pre-determines the path of the crack. They found that these shear cracks accelerate towards a particular speed of $\sqrt{2}C_s$, under steady-state conditions, as predicted by theory. Likewise, a line of discontinuity or shock wave develops at an angle of 45° with respect to the plane of the crack. These findings illustrate that intersonic crack propagation is primarily related to the propagation mode and that the phenomenon occurs as long as enough energy is delivered to the crack tip.

In the case of unidirectional fiber composites, a weak fracture plane typically develops at the interface between matrix and fibers. Furthermore, due to material elastic anisotropy, wave speeds along the fiber direction are very different to the wave speeds in the perpendicular direction. Hence, it was expected that the intersonic crack phenomenon could also occur in these materials as well. Experimental studies on dynamic crack propagation in unidirectional fiber composites were conducted by Zheng and Sun (1995), Lambros and Rosakis (1997), Stout et al. (1998), and Coker and Rosakis (1998, 2001). The work by Coker and Rosakis revealed that asymmetrically loaded (mode II) cracks indeed propagate intersonically at unprecedented speeds of three times the composite shear wave speed and almost the material longitudinal wave speed along the fiber direction. Evidence of large scale frictional contact was also reported. The same findings were computationally predicted by Espinosa et al. (1998a,b), see first page footnote.

Due to the importance of fiber composite materials in civilian and strategic defense applications, it is important to develop tools for detailed finite element analyses of dynamic crack propagation under impact loading. In particular, the examination of conditions for intersonic crack propagation need to be assessed. Likewise, the following features need further research: (1) threshold impact energy above which intersonic crack propagation is possible in unidirectional fiber composites, (2) effects of plastic zone around the crack tip, (3) formation of shock waves, (4) characteristics of contact zone behind crack tip, (5) effect of friction in the contact zone, and (6) characterization of intersonic crack propagation in terms of the dynamic J' integral.

To our knowledge, only a limited number of analytical and computational studies, on the subject of dynamic crack propagation in fiber composite materials, were reported in the literature. Among these studies we can mention Huang et al. (1999), Hwang and Geubelle (2000), Kumar and Kishore (1998), Stout et al. (1998), Lo et al. (1993), Sun and Qian (1997), Pandey and Sun (1996), and Sun and Wu (1996). None of these studies included frictional contact behind the crack tip. The present work focuses on studying dynamic crack propagation in unidirectional composites using a cohesive surface formulation and a contact/friction algorithm. Dynamic crack propagation in a unidirectional graphite/epoxy composite plate is studied using the finite deformation anisotropic visco-plastic model, in total Lagrangian co-ordinates, of Espinosa et al. (2001). The contact/interface methodology of Espinosa et al. (1998b) is used to analyze crack propagation. The model is first validated with the analysis results of Xu and Needleman (1996) for dynamic crack propagation along a bimaterial interface. It is then used to study dynamic crack propagation in unidirectional graphite/epoxy composite plates under the influence of varying impact velocities and surface friction characteristics. The dynamic J' integral is evaluated in each case to study the energy associated with the propagating crack tip.

2. Finite deformation anisotropic visco-plasticity model

The simulation of the response of fiber composite materials requires the formulation of large

deformation inelastic constitutive models. Identification of an appropriate yield function and the plastic flow rule to describe the non-linear anisotropic behavior of fiber composite materials is a challenge in itself, see e.g., Sun and Chen (1989), Espinosa et al. (1997), Chen et al. (1997), O'Donoghue et al. (1992), Voyiadjis and Thiagarajan (1995) and Voyiadjis and Thiagarajan (1996), etc. amongst others. Previously, the approach has been to computationally homogenize the directional properties of composite materials. This helps in deriving a formulation applicable for such materials and in facilitating the implementation of a finite element computer program. In contrast, micromechanical models, Aboudi (1989), Paley and Aboudi (1992) and Stout et al. (1998) treat the matrix and fiber materials separately, and derive the overall constitutive relation of a cell using periodicity and traction continuity at the boundary of sub-cells. On one hand, homogenized constitutive relations are simple to use in a finite element code; however, their capability to simulate extensive damage during impact and penetration remains a topic of research. On the other hand, micromechanical cell models can simulate a large extent of damage modes, but they are highly computer intensive. Modeling all the inherent characteristics of fiber composite materials to determine their response at high strain rates remains a formidable challenge. Simplified models have been sought to study selected behavior of these materials, see for instance Lee and Sun (1992) and Lee and Sun (1993). In this work, one of such simple models is employed.

Consider a solid with volume B_0 in the reference configuration, and a deformation process characterized by the mapping $\mathbf{x}(\mathbf{X}, t)$ (see Fig. 2). A material point initially at $\mathbf{X}$ will be located at $\mathbf{x} = \mathbf{X} + \mathbf{u}$ after deformation, in which $\mathbf{u}$ is the displacement vector. A displacement based finite element formulation is obtained from the weak form of the momentum balance or dynamic principle of virtual work. The weak form at time t in total Lagrangian co-ordinates, i.e., referred to the reference configuration, is given by

$$\int_{B_0} [\nabla_0 \mathbf{P}^0 + \rho_0(\mathbf{b}_0 - \mathbf{a})] \cdot \eta \, \mathrm{d}B_0 = 0 \tag{1}$$

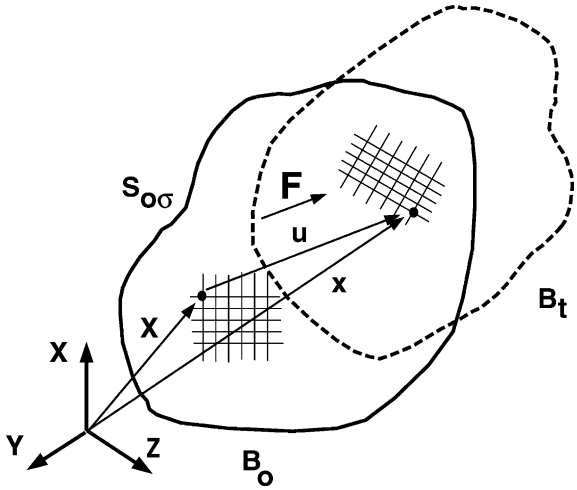

Fig. 2. Total Lagrangian continuum model.

$$\int_{B_0} \mathbf{P}^0 : \nabla_0 \eta \, \mathrm{d}B_0 - \int_{B_0} \rho_0(\mathbf{b}_0 - \mathbf{a}) \cdot \eta \, \mathrm{d}B_0 - \int_{S_{0\sigma}} \mathbf{t} \cdot \eta \, \mathrm{d}S_0 = 0 \tag{2}$$

where $\mathbf{P}^0$ is the first Piola–Kirchhoff stress tensor at time t; $\mathbf{b}_0$, $\mathbf{a}$, and $\mathbf{t}$ are the body force vector, acceleration vector, and boundary traction vector on volume B_0 and boundary $S_{0\sigma}$, respectively. Virtual displacement field η is assumed to be admissible, and ρ_0 represents the material density per unit volume in the reference configuration. The symbol ∇_0 denotes the material gradient with respect to the reference configuration, and ':' is used to denote the inner product between second order tensors, e.g., $\mathbf{A} : \mathbf{B} \equiv A_{ij}B_{ji}$, where the summation convention on repeated indices is implied.

Alternately, the weak form of the momentum balance, in terms of spatial quantities, is given by

$$\int_{B_0} \tau : \nabla^{\mathrm{s}} \eta \, \mathrm{d}B_0 - \int_{B_0} \rho_0(\mathbf{b}_0 - \mathbf{a}) \cdot \eta \, \mathrm{d}B_0 - \int_{S_{0\sigma}} \mathbf{t} \cdot \eta \, \mathrm{d}S_0 = 0 \tag{3}$$

in which superscript s stands for the symmetric part of the tensor, $\tau = \mathbf{F}\mathbf{P}^0$ is the Kirchhoff stress, $\mathbf{F}$ is the deformation gradient at time t, and ∇ is the spatial deformation tensor. As Eq. (3) shows, the equation of motion in its weak form states that

the work done by the stresses τ over strains $\nabla^s\eta$ equals the work done by applied body forces, inertia forces, and surface tractions. In the absence of the body force, the above equation reduces to the following discrete equation, $\mathbf{M}\ddot{\mathbf{U}} = -(\mathbf{f}_{\mathbf{int}} + \mathbf{f}_{\mathbf{surf}})$, where $\mathbf{M}$ is the global mass matrix, $\ddot{\mathbf{U}}$ is the global acceleration vector, $\mathbf{f}_{\mathbf{int}}$ is the internal force vector and $\mathbf{f}_{\mathbf{surf}}$ is the equivalent surface force vector resulting from integration of the surface traction vector. The impactor as well as the target are discretized spatially into six node quadratic triangular elements. The mass of triangular elements is lumped at their nodes to obtain the global lumped mass matrix $\mathbf{M}$. Details on the numerical integration of the above equations can be found in Espinosa et al. (1998b).

The constitutive response of the fiber composite is formulated in terms of the Green–Lagrange strain tensor $\mathbf{E}$ and the work conjugate second Piola–Kirchhoff stress tensor $\mathbf{S}$, Espinosa et al. (2001). The Green–Lagrange strain rate tensor at time step $t + \Delta t$, is given as,

$$\dot{E}_{ij} = \frac{1}{2\Delta t}\left[(F_{ki}F_{jk})_{t+\Delta t} - (F_{ki}F_{jk})_t\right] \tag{4}$$

where F_{ij} is the deformation gradient and Δt is the incremental time step. All quantities in the above equation are defined in the global co-ordinates. The second Piola–Kirchhoff's stress rate tensor is given by a hyperelastic constitutive law, which in rate form is given by,

$$\dot{S}_{ij} = C_{ijkl}\dot{E}^{\mathrm{e}}_{kl} \tag{5}$$

where C_{ijkl} is the elastic anisotropic material stiffness constitutive tensor in the global co-ordinates and $\dot{E}^{\mathrm{e}}_{ij}$ is the elastic component of the Green–Lagrange strain rate tensor. As explained by Espinosa et al. (1998b), the Kirchhoff stress τ and second Piola–Kirchhoff stress $\mathbf{S}$ are related through the relation $\tau = \mathbf{FSF^T}$. In the case of anisotropic materials, the elastic constitutive matrix ($\mathbf{C_l}$) is defined in the local co-ordinate system of the lamina. It is transformed to $\mathbf{C} = \mathbf{T^T C_l T}$ to obtain the constitutive matrix in the global co-ordinates following standard transformation procedures.

The elastic components of the strain rate tensor are obtained by an additive decomposition of the total Green–Lagrange strain rate, namely,

$$\dot{E}^{\mathrm{e}}_{ij} = \dot{E}_{ij} - \dot{E}^{\mathrm{p}}_{ij} \tag{6}$$

In the above equation, $\dot{E}^{\mathrm{p}}_{ij}$ is the plastic strain rate which is based on the associative flow rule,

$$\dot{E}^{\mathrm{p}}_{ij} = \dot{\lambda}\frac{\partial f}{\partial S_{ij}} \tag{7}$$

Here, f is the flow potential and $\dot{\lambda}$ is the plastic rate proportionality factor. The inelastic behavior of the composite is modeled based on a flow potential quadratic in the second Piola–Kirchhoff's stress tensor, as proposed by Espinosa et al. (1997), i.e.,

$$\begin{aligned} 2f(S_{ij}) = {} & a_{11}S_{11}^2 + a_{22}S_{22}^2 + a_{33}S_{33}^2 + 2a_{12}S_{11}S_{22} \\ & + 2a_{13}S_{11}S_{33} + 2a_{23}S_{33}S_{22} + 2a_{44}S_{23}^2 \\ & + 2a_{55}S_{13}^2 + 2a_{66}S_{12}^2 \end{aligned} \tag{8}$$

For unidirectional fiber reinforced carbon/epoxy composite with 2–3 isotropy, 1 direction being the fiber direction and 2 normal to it in the lamina plane, the above yield function reduces to, Weeks and Sun (1996) and Weeks and Sun (1998),

$$f(S_{ij}) = \tfrac{1}{2}S_{22}^2 + a_{66}S_{12}^2 \tag{9}$$

Defining an effective stress as,

$$\bar{S} = \sqrt{3f} \tag{10}$$

and using Eqs. (8) and (10), the rate of plastic work is given by,

$$\dot{W}^{\mathrm{p}} = S_{ij}\dot{E}^{\mathrm{p}}_{ij} = \bar{S}\dot{\bar{E}}^{\mathrm{p}} \tag{11}$$

The proportionality factor of Eq. (7) is obtained as

$$\dot{\lambda} = \frac{3\dot{\bar{E}}^{\mathrm{p}}}{2\bar{S}} \tag{12}$$

where $\dot{\bar{E}}^{\mathrm{p}}$ is the effective plastic strain rate. The effect of strain rate and temperature can be modeled by defining the material strength in terms of an effective stress which includes temperature and rate terms, namely,

$$\dot{\bar{E}}^{\mathrm{p}} = \dot{\bar{E}}^{\mathrm{p}}_0\left[\frac{\bar{S}}{g(\bar{E}^{\mathrm{p}}, T)}\right]^m \quad \text{if} \quad \bar{S} > g(\bar{E}^{\mathrm{p}}, T) \tag{13}$$

$$g(\bar{E}^{\mathrm{p}}, T) = \bar{S}_y\left[1 - \left(\frac{T - T_0}{T_{\mathrm{m}} - T_0}\right)^{\alpha}\right] \tag{14}$$

in which $\bar{S}_y$ is the flow stress at reference plastic strain rate $\dot{\bar{E}}_0^{\mathrm{p}}$ and temperature T_0. T_{m} is the glass transition temperature of the matrix material. $\bar{S}$ is the flow stress at the current effective plastic strain rate $\dot{\bar{E}}^{\mathrm{p}}$ and temperature T. m and α are the rate and temperature sensitivity exponents, respectively. The reference flow stress $\bar{S}_y$ is defined by an experimentally found power law,

$$\bar{S}_y = \left(\frac{\bar{E}^{\mathrm{p}}}{A}\right)^{1/n} \tag{15}$$

in which n is the strain hardening exponent. A summary of the constitutive equations in discrete form is given in Table 1. Other functional forms for g can be used, for instance, functions involving hyperbolic sines that are typical of polymer matrices.

To account for a nonlinear response during unloading, another power law is used. The coefficients used in the yield potential, given above, can be identified from off-axis and out-of-plane shear tests as explained in Espinosa et al. (2001).

Table 1
Summary of constitutive equations

$$\dot{S}_{t+\Delta t} = C\dot{E}^{\mathrm{e}}_{t+\Delta t}$$

$$\dot{E}_{t+\Delta t} = \dot{E}^{\mathrm{e}}_{t+\Delta t} + \dot{E}^{\mathrm{p}}_{t+\Delta t}$$

$$\dot{E}^{\mathrm{p}}_{t+\Delta t} = \dot{\lambda}\frac{\partial f}{\partial S_{t+\Delta t}} = \frac{3\dot{\bar{E}}^{p}}{2\bar{S}}\frac{\partial f}{\partial S_{t+\Delta t}} = \dot{\bar{E}}^{\mathrm{p}}_{t+\Delta t}N_{t+\Delta t}$$

$$N_{t+\Delta t} = \frac{3}{2}\frac{\frac{\partial f}{\partial S_{t+\Delta t}}}{\bar{S}_{t+\Delta t}} = \frac{3}{2\bar{S}}\begin{bmatrix} 0 & 2a_{66}S_{12} & 2a_{55}S_{13} \\ 2a_{66}S_{12} & 0 & 2a_{44}S_{23} \\ 2a_{55}S_{13} & 2a_{44}S_{23} & S_{33} \end{bmatrix}_{t+\Delta t}$$

$$\bar{S}_{t+\Delta t} = \sqrt{3f_{t+\Delta t}(S_{ij})_{t+\Delta t}}$$

$$g(\bar{E}^{\mathrm{p}}_{t+\Delta t}, T) = \bar{S}_{y,t+\Delta t}\left[1 - \left(\frac{T - T_0}{T_{\mathrm{m}} - T_0}\right)^{\alpha}\right]$$

$$\bar{S}_{y,t+\Delta t} = \left(\frac{\bar{E}^{\mathrm{p}}_{t+\Delta t}}{A}\right)^{\frac{1}{n}}$$

$$\dot{\bar{E}}^{\mathrm{p}}_{t+\Delta t} = \dot{\bar{E}}^{\mathrm{p}}_0\left[\frac{\bar{S}_{t+\Delta t}}{g(\bar{E}^{\mathrm{p}}_{t+\Delta t}, T)}\right]^m$$

3. Contact/interface cohesive law

The cohesive surface formulation has gained prominence in simulating crack initiation, propagation, and fragmentation in brittle materials, Xu and Needleman (1995), Xu and Needleman (1996), Xu (1996), Camacho and Ortiz (1996) and Espinosa et al. (1998a). Geubelle and Baylor (1998), Espinosa et al. (1999) and Espinosa et al. (2001) have shown that a combined model incorporating homogenized constitutive relation for fiber composite materials and cohesive interface elements between lamina can be employed to analyze dynamic delamination in fiber composite materials in agreement with experiments.

In this study, the interface law used to simulate onset and crack propagation is based on a contact/interface approach proposed by Espinosa et al. (1998b) and Espinosa et al. (1999). As shown in Fig. 3, interface elements are embedded along the possible crack path. The tensile and shear tractions developed by the interface element are calculated from the interface cohesive law. This law describes the evolution of these tractions and the coupling between them as a function of relative normal and tangential displacements. The compressive traction, if any, is calculated through the

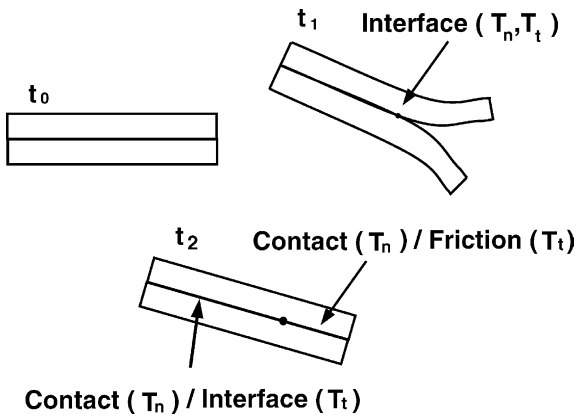

Fig. 3. Interface/contact model with finite kinematics.

impenetrability condition employed in the contact module. Once the effective displacement jump exceeds a specified critical value, the interface element is assumed to have failed, i.e., onset of crack propagation is said to have taken place. The new free surfaces as a result of crack propagation are automatically created. Thereafter, the interaction between the surfaces is described solely by the contact algorithm, which includes frictional effects. The failure of successive interface elements simulates crack extension as in Xu and Needleman (1996).

A detailed formulation of the interface element and cohesive laws can be found in Espinosa et al. (1999), and Espinosa and Zavattieri (2002a,b). Instead of a zero thickness 4-noded quadrilateral element used by Espinosa et al. (1999), a zero thickness 6-noded interface element, as shown in Fig. 4, is used in the present work. When inserted at the boundary of 6-noded triangular elements used in the discretization of the plates, the response of the interface element becomes more consistent to the discrete body response surrounding it. The shape functions of the one-dimensional 3-noded differential element are given in a standard textbook on finite element methods. Integration of surface traction to determine nodal force vector is carried out using a 3-point Gauss quadrature rule.

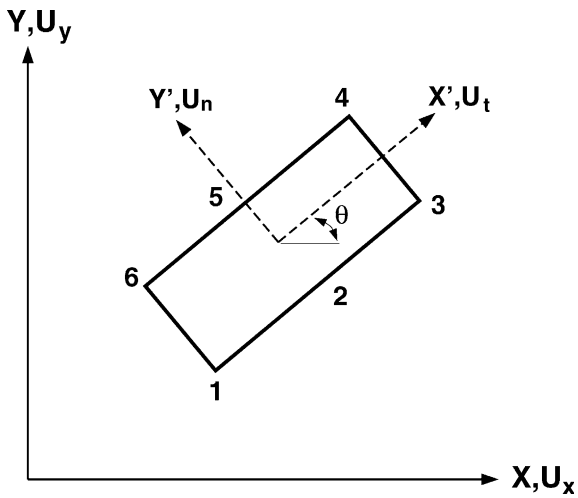

Fig. 4. Six-noded interface element showing definition of global and local co-ordinates.

The interface law II, Espinosa et al. (1999), is used to define the evolution of normal and tangential traction and the coupling between them as a function of the relative normal and tangential displacement jumps, respectively. The equivalent traction $\tau(\lambda)$ is given in terms of a non-dimensionalized effective displacement jump parameter λ defined as:

$$\lambda = \sqrt{\left(\frac{U_n}{\delta_n}\right)^2 + \left(\frac{U_t}{\delta_t}\right)^2} \tag{16}$$

where U_n and U_t are the actual normal and tangential displacement jumps at the interface. δ_n and δ_t are the critical normal and tangential displacement jumps at which the interface fails or crack initiates in pure normal or pure shear mode, respectively. The value of $\lambda = 0$ signifies the unstressed state of the element and $\lambda = 1$ signifies total failure. As described earlier, the tensile and shear state of the interface element for $\lambda \leqslant 1$ is determined from the interface cohesive law while the compressive state is determined from the contact law. After complete debonding, i.e., $\lambda = 1$, the interface is characterized solely by the contact law. The procedure adopted in the explicit integration is summarized in Table 2.

It is assumed here that the interface traction evolves reversibly up to a value $\lambda = \lambda_c$, similar to the state of elastic loading and unloading in materials. Beyond λ_c, unloading from a state λ_u and subsequent re-loading take place irreversibly. The cohesive law used in the analyses is plotted in Fig. 5. The value of λ_c is selected such that the wave speeds in the material with interfaces is the same as the ones in the material without interfaces during reversible loading. The interface law, so derived, is given as,

Table 2
Contact and interface calculations based on interface traction

Load	State	T_n	T_t
Tension-shear	$\lambda < 1$	Interface	Interface
	$\lambda \geqslant 1$	Contact	Open
Compression-shear	$\lambda < 1$	Contact	Interface
	$\lambda \geqslant 1$	Contact	Friction

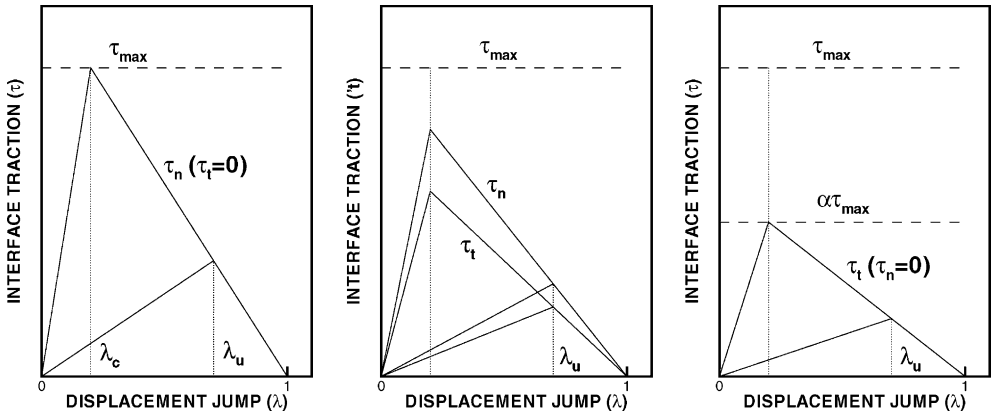

Fig. 5. Cohesive law: evolution of interface traction in loading and unloading.

(i) for loading and unloading in the range $0 \leqslant \lambda \leqslant \lambda_c$:

$$\tau_n = \frac{U_n}{\delta_n}\frac{\tau_{max}}{\lambda_c}; \quad \tau_t = \alpha\frac{U_t}{\delta_t}\frac{\tau_{max}}{\lambda_c}, \tag{17}$$

where τ_n and τ_t are the normal and tangential tractions corresponding to the normal and tangential displacement jump U_n and U_t respectively, τ_{max} is the maximum normal traction beyond which failure initiates and α is a mode mixity parameter;

(ii) for loading in the range $\lambda_c < \lambda \leqslant 1$:

$$\tau_n = \tau_{max}\frac{U_n^c}{\delta_n}\frac{1-\lambda}{1-\lambda_c}; \quad \tau_t = \alpha\tau_{max}\frac{U_t^c}{\delta_t}\frac{1-\lambda}{1-\lambda_c} \tag{18}$$

where U_n^c and U_t^c are the normal and tangential displacement jumps attained at $\lambda = \lambda_c$,

(iii) for unloading and reloading in the range $0 \leqslant \lambda \leqslant \lambda_u$, where $\lambda_u > \lambda_c$ is the last value of λ from where irreversible unloading took place:

$$\tau_n = \frac{U_n}{\delta_n}\frac{\tau_{max}}{\lambda_u}; \quad \tau_t = \alpha\frac{U_t}{\delta_t}\frac{\tau_{max}}{\lambda_u} \tag{19}$$

(iv) for loading in the range $\lambda_u < \lambda \leqslant 1$:

$$\tau_n = \tau_{max}\frac{U_n^u}{\delta_n}\frac{1-\lambda}{1-\lambda_u};$$
$$\tau_t = \alpha\tau_{max}\frac{U_t^u}{\delta_t}\frac{1-\lambda}{1-\lambda_u} \tag{20}$$

where U_n^u and U_t^u are the normal and tangential displacement jumps attained at $\lambda = \lambda_u$ during reverse loading.

In the absence of Mode II deformation, the area under the $\tau_n - \delta_n$ curve gives the Mode I critical strain energy release rate G_{Ic}, which can be written as:

$$G_{Ic} = \tfrac{1}{2}\delta_n\tau_{max} \tag{21}$$

Similarly, in the absence of Mode I deformation, the area under the $\tau_t - \delta_t$ curve gives the Mode II critical strain energy release rate G_{IIc}, which can be written as:

$$G_{IIc} = \tfrac{1}{2}\alpha\delta_t\tau_{max} \tag{22}$$

Hence, if $\delta_n = \delta_t$, α defines the ratio G_{IIc}/G_{Ic} (Espinosa et al., 1999).

As mentioned earlier, failure of successive interface elements simulates crack propagation. For this purpose, the time of failure of each Gauss point along interface elements is recorded. This data provides the crack length history. The crack speed is obtained by differentiating the crack length data using a four-point backward difference method. As expected, the crack speed so obtained will have oscillations depending on the element size.

4. Dynamic J' integral

The dynamic J' integral formulation was developed to establish a single parameter to characterize the dynamic stress field and energy associated with a dynamically growing crack, Nakamura et al. (1995), Xu and Needleman (1996) and Kumar and Kishore (1998). It is not the purpose here to review the development of the formulation of J' and its numerous versions for different loading conditions,

such as elasto-static, elasto-dynamic, elasto-plastic, and elasto-plastic-dynamic loading of the crack tip. In the present study, for a local co-ordinate system x_i where x_1 is aligned parallel to the direction of crack propagation, the dynamic J' integral is evaluated from a closed contour around the crack tip as discussed in Atluri (1982), Nakamura et al. (1985), Carpenter et al. (1986), Moran and Shih (1987) and Nishioka (1994),

$$J' = \lim_{\Gamma_\epsilon \to 0} \int_\Gamma \left[(W+T)n_1 - P_{ji}\frac{\partial U_i}{\partial X_1} n_j \right] \mathrm{d}\Gamma \tag{23}$$

$$J' = \int_{\Gamma_0} \left[(W+T)n_1 - P_{ji}\frac{\partial U_i}{\partial X_1} n_j \right] \mathrm{d}\Gamma + \int_{A_0} \left[\rho \frac{\partial^2 U_i}{\partial t^2}\frac{\partial U_i}{\partial X_1} - \rho \frac{\partial U_i}{\partial t}\frac{\partial^2 U_i}{\partial X_1 \partial t} \right] \mathrm{d}A \tag{24}$$

where P_{ij} are the ij components of the first Piola–Kirchhoff stress tensor, ρ is the material density, W and T are the stress–work density and the kinetic energy density per unit initial volume defined as:

$$W = \int_0^t S : E \,\mathrm{d}t = \sum_0^t S_{ij}\Delta E_{ij} \tag{25}$$

$$T = \frac{1}{2}\rho \left(\frac{\partial U_i}{\partial t} \right)^2 \tag{26}$$

and n_i is the normal to contour Γ. Γ_ϵ is the vanishing inner contour around the crack tip, taken as the crack tip itself in the present analyses. Γ_0 is the outer contour including the crack faces, i.e., $\Gamma_0 = \Gamma_C^+ + \Gamma + \Gamma_C^-$. A_0 is the area between the inner and outer contours. Since the inner contour is taken at the crack tip, A_0 becomes the area enclosed by the outer contour.

Using the weight function q, the dynamic J' integral is calculated as:

$$J' = \int_{A_0} \left[P_{ji}\frac{\partial U_i}{\partial X_1}\frac{\partial q_k}{\partial X_j} - (W+T)\frac{\partial q_k}{\partial X_k} \right] \mathrm{d}A_0 + \int_{A_0} \left[P_{ji}\frac{\partial^2 U_i}{\partial X_j \partial X_k} - \frac{\partial W}{\partial X_k} \right] q_k \,\mathrm{d}A_0 + \int_{A_0} \left[\rho \frac{\partial^2 U_i}{\partial t^2}\frac{\partial U_i}{\partial X_1} q_k. - \rho \frac{\partial U_i}{\partial t}\frac{\partial^2 U_i}{\partial X_1 \partial t} q_k \right] \mathrm{d}A_0 \tag{27}$$

All integrals are carried out over the area enclosed by the outer contour Γ_0. As $P_{ji}\partial U_i/\partial X_j$ is the energy term, the contribution by the second integral is neglected in the present analyses. Various schemes for selecting the weighting function q has been used in the past (Carpenter et al., 1986). In the present analyses, q is unity from the crack tip up to the node just before the outer contour, then reduces linearly to zero at the outer contour. Also, the component of q normal to the crack front and interface elements are taken as zero.

The dynamic J' integral is evaluated for a number of contours using contour integrals as well as the weight function area integral. As per conventional practice, the parts Γ_{C^+} and Γ_{C^-} are assumed parallel to each other and traction-free. Due to reasons of possible large rotation of the crack front and contact zone behind the crack tip, these crack fronts are not neglected. In order to account for these two crack faces, contours are formed through the nodes of 6-noded quadrilateral elements, instead of forming through the integration points (Li and Shih (1985)). For calculating J' based on the contour integral, the stress–work density W and P_{ij}, obtained from S_{ij}, are extrapolated to contour nodes from the contributing integration points. However, the calculation of J' from the weight function area integral involves integration over the element's area. Hence, no extrapolation is required in this case and calculation is performed using standard finite element procedures. As shown in the following sections, the J' calculated from the contour integral equation (24) and area integral equation (27) are identical.

5. Analyses

The above model is first validated by comparison with analyses reported in the literature. Then it is used to study dynamic crack propagation in unidirectional carbon fiber reinforced composite materials.

5.1. Model validation by comparison with literature results

Our integrated model is used to analyze dynamic crack propagation along bimaterial inter-

faces and the results are compared with the literature data (Xu and Needleman, 1996). The problem being analyzed is shown in Fig. 6 on the left (Fig. 1a in Xu and Needleman (1996)). A bimaterial plate of width 6.1 mm and height 5.6 mm with a central crack of length 0.5 mm is restrained at the bottom and loaded with a specified constant velocity at the top. Two cases are considered. In one case, referred to as PMMA/MA the top half plate is made of PMMA and bottom half plate is made of an assumed material called A. The specified constant velocity in this case is $V = 30$ m/s. In the other case, referred to as MA/PMMA, the two material halves are opposite to the first case and the applied velocity is $V = 11.73$ m/s. Due to symmetry, only half of the plate is analyzed in each case. The displacement and velocity boundary conditions used in the two elastic analyses are shown in Fig. 6 in the center. In both cases, the velocity rises linearly from time zero to its maximum value at 0.1 μs as shown in Fig. 6 on the right side. The finite element mesh with two zoomed views at the pre-notch tip and the five contours considered for the J' calculation are shown in Fig. 7. The mesh used for the analyses has 6712 nodes, 3214 triangular elements and 89 interface elements with average length of interface elements as 0.03 mm. The properties of the two materials and interface, as used in the analyses, are given in Table 3.

The crack speed obtained from the simulations are shown in Fig. 8. The analyses results of Xu and Needleman (1996) are also plotted in the same figure for comparison. It is seen that the present model is able to predict crack extension time and crack speed in good agreement with the literature data, even though the latter used a very fine mesh with an interface element length of 0.004 mm. The far field path independent integrals calculated at the 5th contour for the two cases are shown in Fig. 9 and compared with the literature results. It is seen that the J' value for MA/PMMA agrees well with the literature data. For the PMMA/MA case, there is qualitative agreement, but the J' value obtained in the present work differs from the literature data. The observed differences in the crack speed or J' may be due to the coarser mesh used in the present analyses, differences in interface cohesive law as used in the analysis, difference in defining the onset of crack extension, as well as to the more refined contact/interface methodology used in the present analysis. In the present investigation, the crack is said to begin extension as soon as an interface element fails, i.e., the displacement jump at all the three integration points reaches the critical displacement jump, i.e., $\lambda = 1$. Xu and Needleman (1996) define the crack tip position where the displacement jump is five times the critical displacement jump. Contrary to the present model, their approach ignores contact behind the crack tip and the initial slope of the cohesive law is quite different. The compressive part of their interface cohesive law allows some interpenetration at the interface, ahead as well as behind the crack tip. The contact/interface approach of the present model enforces impenetrability strictly and hence

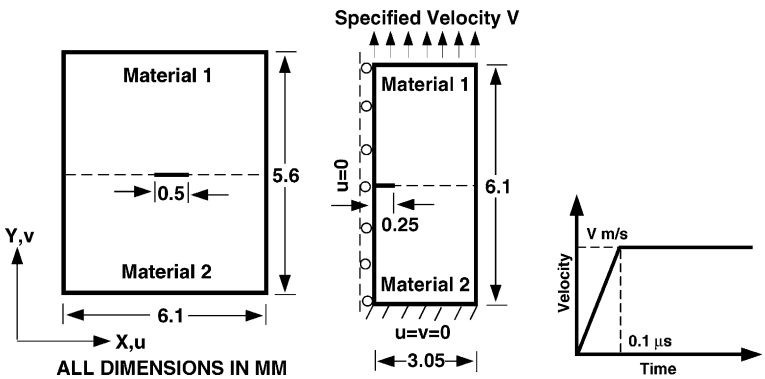

Fig. 6. Problem geometry: model validation with analyses data for dynamic crack propagation along a bimaterial interface.

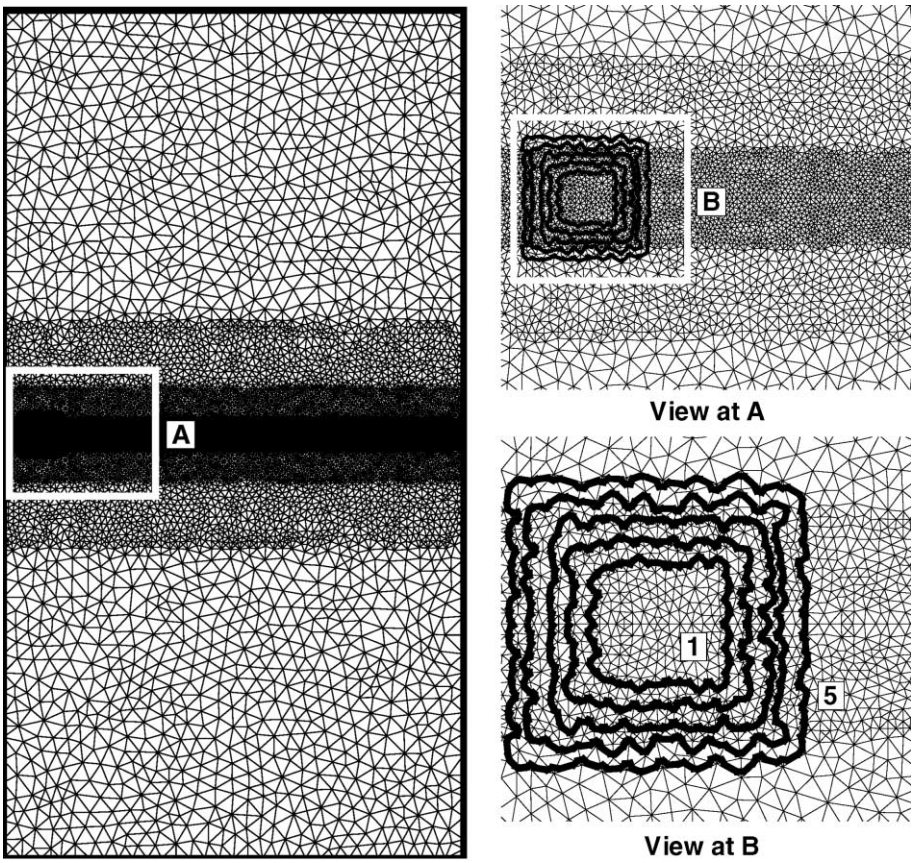

Fig. 7. Finite element mesh and contours used in the analyses.

Table 3
Materials properties for validation with literature analyses

Materials properties		Units
PMMA	Material A	
Density		
$\rho_0 = 1190.0$	$\rho_0 = 5950.0$	kg/m^3
Elastic properties		
$E = 3.24$	$E = 6.44$	GPa
$\nu = 0.35$	$\nu = 0.15$	
$C_s = 1004$	$C_s = 686$	m/s
$C_R = 938$	$C_R = 616$	m/s
Interface properties		
$T_{max} = 162$		MPa
$\delta_n = 2.1753$		μm
$\delta_t = 0.933$		μm
$\alpha = 2.3315$		
$\lambda_c = 0.05$		

is bound to modify the crack tip stress field. Nevertheless, the agreement obtained even with the coarse mesh used in the present analyses is reasonable.

5.2. Unidirectional fiber composite plate loaded in mode II

The above analyses show that the proposed model predicts the phenomenon of dynamic crack propagation in close agreement with analyses results taken from literature. Detailed analyses are carried out next to study the phenomenon of dynamic crack propagation in an unidirectional graphite/epoxy composite. The problem definition is shown in Fig. 10. A pre-notched unidirectional composite plate of total width 250 mm and height 300 mm is considered. The fiber direction is taken

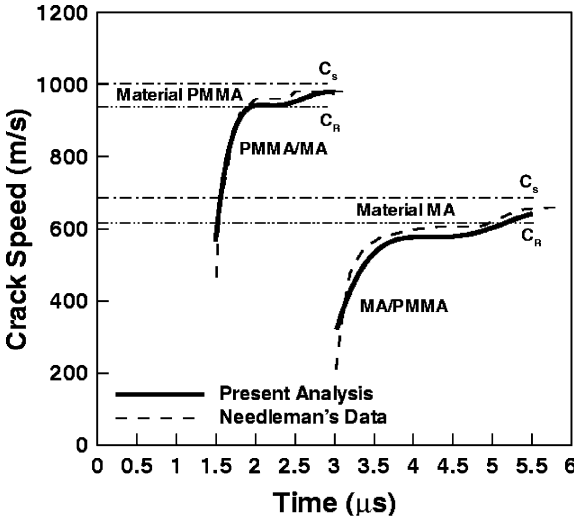

Fig. 8. Crack speed predicted by present analyses and comparison with literature data.

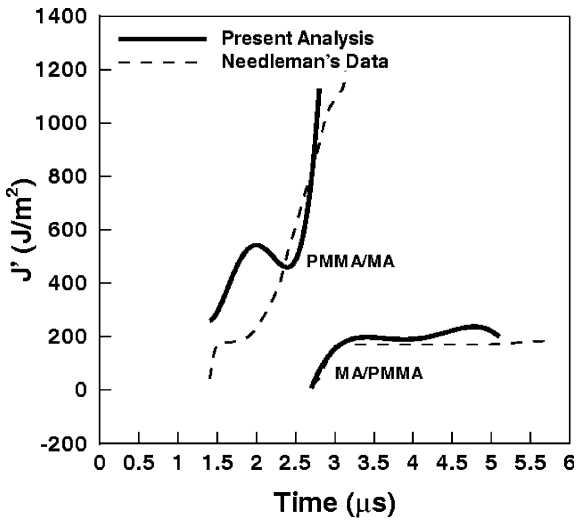

Fig. 9. Plot of dynamic integral, J', history and comparison with literature data.

parallel to the **X**-direction. The length and maximum opening of the pre-notch, parallel to the **X**-axis, are 25 and 1.5 mm, respectively. The plate is impact loaded off-center on the face opposite to the pre-notch face. The loading is provided by specifying a constant velocity in the negative **X**-direction over an assumed projectile diameter. The projectile diameter in all the analyses is kept constant as 50 mm. In order to minimize numerical oscillation, it is assumed that the velocity increases to the maximum over a time period of 1.0 μs and remains constant thereafter at the specified value of **V** m/s. The problem geometry and boundary conditions so defined are consistent with the experimental set up reported in Coker and Rosakis (2001). In our calculations the plate dimensions are slightly larger; however, this difference does not modify the physics of the problem and, as it will be discussed later, most of the features observed experimentally are captured in our simulations.

Since all materials and interface properties are not available for one particular graphite/epoxy composite, they are judiciously selected from two sources. Elastic and anisotropic flow potential data for the unidirectional composite plate are taken from Weeks and Sun (1996), while the interface properties are taken from Stout et al. (1998). It is assumed that this combination of mechanical and interface properties provides an idealized unidirectional carbon/epoxy composite for the purpose of studying the phenomenon of dynamic crack propagation. The material properties used in the analyses are summarized in Table 4. Note that these elastic constants are not the same to the ones reported in Coker and Rosakis (2001), in fact the work here reported was done simultaneously and independently. Hence, the numerical analyses here reported show that intersonic crack propagation is a phenomenon that may occur in a variety of unidirectional fiber composites.

The top and bottom half of the composite plate are discretized into 6-noded quadratic triangular elements, while 6-noded quadratic interface elements are embedded between the two halves. As shown on the left in Fig. 10, crack extension initiates at the pre-notch tip and is allowed to propagate up to a total width of 200 mm. The last 50 mm width of the plate is considered bonded without any interface elements to avoid interface failure from the impact face. The finite element mesh size is a minimum around the crack path and gradually increased towards the top/bottom and right side of the plate. The mesh has 52,032 nodes, 25,602 triangular elements and 295 interface elements. The average size of the quadratic

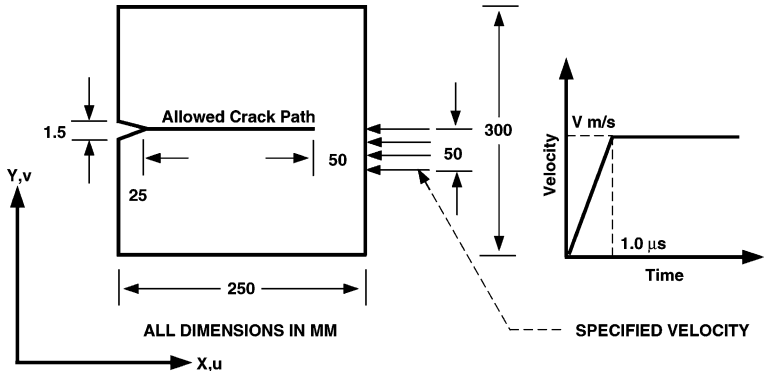

Fig. 10. Dynamic crack propagation in unidirectional fiber reinforced composite—problem definition (left) and specified impact velocity (right).

Table 4
Materials properties of unidirectional carbon/epoxy composite

Materials properties			Units
Properties	Symbol	Value	
Density	ρ_0	1580	kg/m^3
Elastic properties	C_{11}	131.83	GPa
	$C_{22} = C_{33}$	13.90	GPa
	$C_{44} = C_{55}$	6.00	GPa
	C_{66}	3.45	GPa
	$C_{12} = C_{21}$	6.68	GPa
	$C_{13} = C_{31}$	6.68	GPa
	$C_{23} = C_{32}$	6.98	GPa
Stress wave speeds	C_l	9134	m/s
	C_s	1949	m/s
	C_R	1811	m/s
Yield function	a_{66}	2.0	–
Plastic flow properties	$\bar{S}_0$	1.00	Pa
	For $\bar{E}_0^p \leqslant 0.76\%$:		
	$A = 1.26 \times 10^{-44}$		Pa
	$n = 5.1$		–
	For $\bar{E}_0^p > 0.76\%$:		
	$A = 1.76 \times 10^{-72}$		Pa
	$n = 8.5$		–
Flow rate properties	$\dot{\bar{E}}_0^p$	1.0×10^{-5}	s^{-1}
	m	40.0	–
Interface cohesive law parameters	T_{max}	85.00	MPa
	δ_n	7.06	μm
	δ_t	17.70	μm
	α	1.20	–
	λ_c	0.01	–

interface elements, along the allowed crack path, is 0.1 mm. The full plate mesh with two zoomed views and one enlarged view at the pre-notch tip are shown in Fig. 11 together with the five contours used to evaluate the dynamic path independent integral J'. Starting from the nearest contour to the crack tip, contours are numbered serially outwards as shown in the bottom plot of Fig. 11.

Analyses are carried out at five different impact velocities (**V**) of 5, 10, 20, 30 and 40 m/s and for different coefficients of friction along the crack face behind the propagating tip. The crack faces are assumed frictionless for the impact velocities of 5, 10 and 20 m/s. Whereas, the cases of $\mathbf{V} = 30$ and 40 m/s are analyzed for both the frictionless case as well as with friction coefficients of 0.5, 1, 5 and 10. It was found that propagating crack interacts with the stress field generated at the beginning of the bonded interface (last 50 mm of the plate width). This interaction modifies the crack tip stress field and the features of crack propagation. For this reason, analyses results are discussed for a maximum crack extension of 150 mm, i.e., while the interaction is not present. Table 5 summarizes the various performed analyses including impact velocity and friction coefficient. A discussion of the results is given in the following sections.

5.2.1. Crack length and crack speed

Fig. 12 shows the evolution of crack length (left) and crack speed (right) obtained from analyses corresponding to a frictionless crack wake. Crack extension initiates at 58.4, 51.6, 36.1, 32.4 and 31.2 μs, when the composite plate is impacted at velocities of 5, 10, 20, 30 and 40 m/s, respectively. The

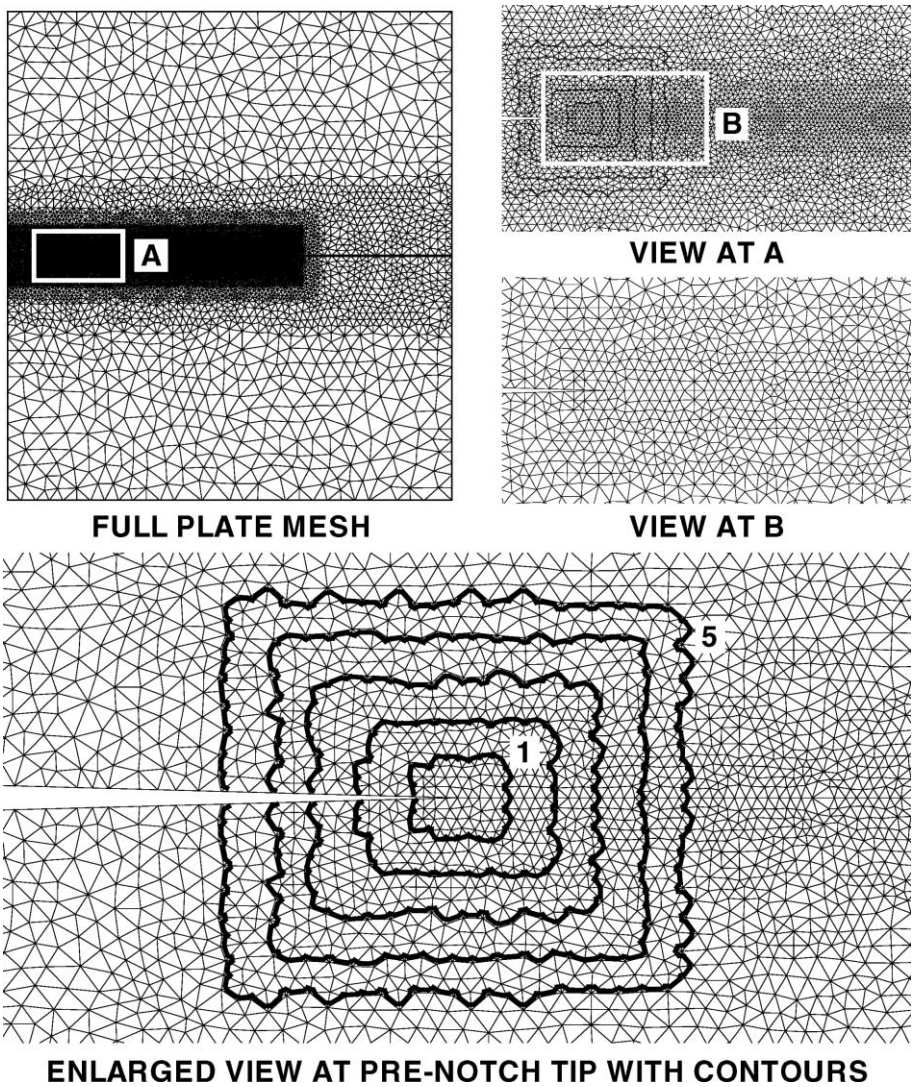

Fig. 11. Finite element mesh and contours for J' calculation used in the analyses.

crack initial speed for the five impact velocities are 209, 382, 658, 1829 and 2146 m/s. After initiation, the crack tip accelerates and attains steady-state speed before stopping or before interacting with boundary waves. The crack acceleration is found to be of the order of $10^7 g$ for impact velocities of 5 and 10 m/s and of the order of $10^9 g$ for impact velocities of 20, 30 and 40 m/s, where g is the gravitational acceleration. The maximum crack speed at the five impact velocities is obtained as 1856, 1879, 7512, 7600, and 7600 m/s.

Table 5
Summary of analyses for fiber composite plate

Analysis	Impact velocity (m/s)	Friction coefficient
1	5.0	0.0
2	10.0	0.0
3	20.0	0.0
4	30.0	0.0, 0.5, 1.0
5	30.0	5.0, 10.0
6	40.0	0.0, 0.5, 1.0
7	40.0	5.0, 10.0

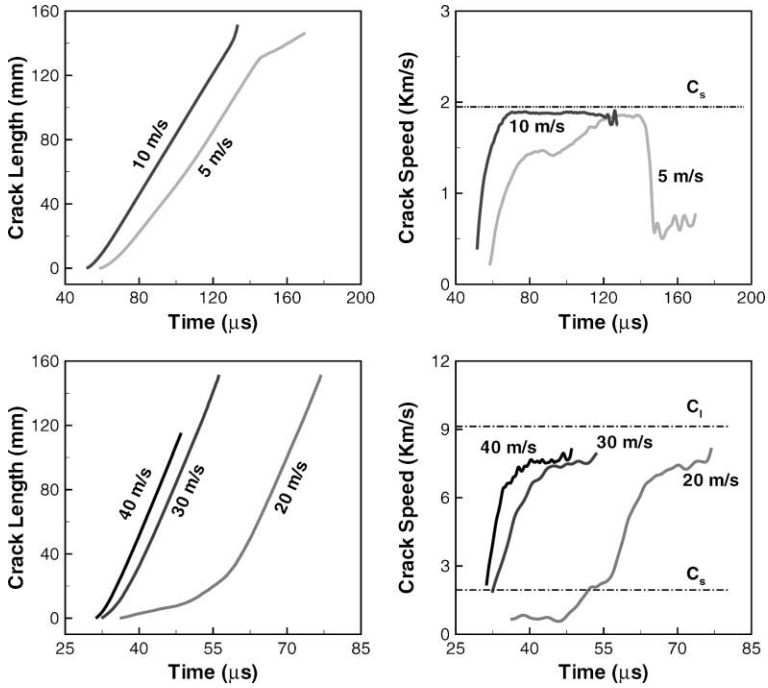

Fig. 12. Evolution of crack length (left) and crack speed (right) at different impact velocities and frictionless crack front.

The above results show that the present analyses predict intersonic crack propagation in the unidirectional fiber composite when the impact velocity exceeds a given threshold. At the lowest 5 m/s impact velocity, the crack accelerates after the onset of extension and attains a velocity of about 1465 m/s. This state is not a steady state and the crack speed first starts reducing. Then, it again starts increasing gradually and attains the steady state at 1856 m/s, which is 95% of the shear wave speed (1949 m/s) of the material. At this impact velocity, the crack tip deaccelerates before reaching the end of the allowable path. At 10 m/s impact velocity, the crack tip accelerates after initiation, and when it attains a maximum speed. Basically, the crack reaches a steady state with an average speed of 1879 m/s, which is 96% of the shear wave speed. Fig. 12 shows a different behavior when the impact velocity is 20 m/s. After initiation, the crack speed remains almost steady at 766 m/s for 10 μs and then accelerates to a speed of 2068 m/s, thus crossing the shear wave speed threshold of the material. Then, it accelerates once more and attains a near steady-state speed of 7512 m/s. Thus, the initiation speed for the 5, 10 and 20 m/s impact velocity remains below the shear wave speed and the crack enters the intersonic regime when the impact velocity reaches 20 m/s. On the contrary, the initiation speed at 30 and 40 m/s impact velocities is above the Rayleigh wave speed (1811 m/s) and 94% and 110% of the shear wave speed of the material, respectively. The maximum steady-state crack speed is found to be 7600 m/s, for both impact velocities, which is 3.9 times the shear wave speed and 83% of the longitudinal wave speed of the material.

The above results show that crack extension speed and maximum crack speed, in sub-sonic regime, monotonically increase with the increase in impact energy. The impact velocity of 10 m/s is found to be the limit beyond which the dynamic crack propagation becomes intersonic. The crack attains a steady state in the intersonic regime and the maximum speed is approximately the same for the three impact velocities of 20, 30 and 40 m/s as considered in the analyses. Thus, the possibility of intersonic crack propagation in unidirectional fiber composites is here established beyond an im-

pact velocity of 10 m/s for assumed steel impactor, 50 mm in diameter, and composite properties. The crack speed attains a maximum of 83% of the longitudinal wave speed, as the impact velocity or imparted energy, exceeds a threshold. These features are in close agreement with the analytical predictions of Huang et al. (1999) in which a critical crack velocity is identified, in the steady-state regime, as the only velocity for which the energy delivered to the crack tip is non-vanishing and finite. The stress wave phenomena influencing crack extension and dynamic propagation is discussed next.

5.2.2. Stress wave history

The pre-notch tip stress and deformation fields, onset of crack extension and observed variation in crack speed are here discussed in terms of stress wave propagation within the plate. Upon asymmetric impact, compressive, as well as shear stress waves, are generated in the lower half of the plate. The waves travel in the **X**-direction towards the pre-notch tip. The shape of the two stress waves are similar to the prescribed boundary velocity, i.e., the stress magnitude increases linearly from zero to a maximum. The speed of the stress wave normal to the fiber direction, i.e., in the **Y**-direction, is 2966 m/s. This is approximately one third of the stress wave speed in the fiber direction. As a result, the compressive stress wave develops a front of an expanding cylinder, instead of being spherical as it is the case in homogeneous materials. The longitudinal stress wave in the fiber direction carries with it a compressive transverse stress and shear stress generated due to material Poisson's effect and elastic anisotropy. These stresses, specially the shear stress, appear to have a waveform traveling at the speed of the longitudinal wave speed in the fiber direction. Nevertheless, it should not be confused with the shear wave, which travels at a much smaller speed of 1949 m/s.

The compressive stress wave reaches the pre-notch tip at 24.6 μs. The entire pre-notch tip is loaded in compression at this instant. Moreover, the tip is also loaded in shear, i.e., mode II, due to the material elastic anisotropy and asymmetric impact loading. The compressive stress pulse reaches the traction-free left plate surface at 27.4 μs. At this instant, a release wave as well as a tensile transverse wave are generated. This release wave unloads the material while propagating in the +**X**-direction. It reaches the pre-notch tip at 30.1 μs and loads it further in shear due to the presence of the traction-free pre-notch surfaces. Crack extension depends on the history of the energy delivered to the pre-notch tip. At the lowest impact velocity of 5 m/s, the energy imparted to the tip by the incident wave is not sufficient until the release tensile transverse wave reaches it and starts loading the crack in mode I. At the highest impact velocities of 40 m/s, the shear energy imparted to the pre-notch tip is such that crack extension occurs earlier. The crack extends at 31.2 μs in predominantly mode II.

5.2.3. Features of sub-sonic crack propagation

Fig. 13 shows crack tip state parameters, for an impact velocity of 10 m/s, immediately after the onset of crack extension and during crack propagation at maximum speed. The plots are contours of longitudinal stress in the fiber direction, S_{11}, transverse (normal) stress S_{22}, shear stress SP_{12}, and effective plastic strain E^{p}_{eff}, i.e., $\bar{E}^{p}$. Black arrows show the position of the crack tip. The maximum crack speed in this case is 1879 m/s, which is 96% of the shear wave speed of the composite. The figure shows that at the onset of crack extension, the normal traction is tensile and the tangential tractions across the pre-notch tip is oppositely directed making the shear stress continuous across the crack front. Hence, the crack initiates under mixed-mode loading. As shown later, the normal and tangential tractions at the onset are of the same order of magnitude during mixed-mode loading. At steady state, the normal traction above the crack front is compressive, which unloads the mode I loading, while the shear stress is continuous ahead of the crack tip. This suggests that the crack propagates at steady state in predominantly mode II, which is confirmed in a later discussion of interface traction history. The figure also shows that the area of plastic flow in the material is small and limited to the crack front. The stress field does not present any discontinuity line behind the crack tip.

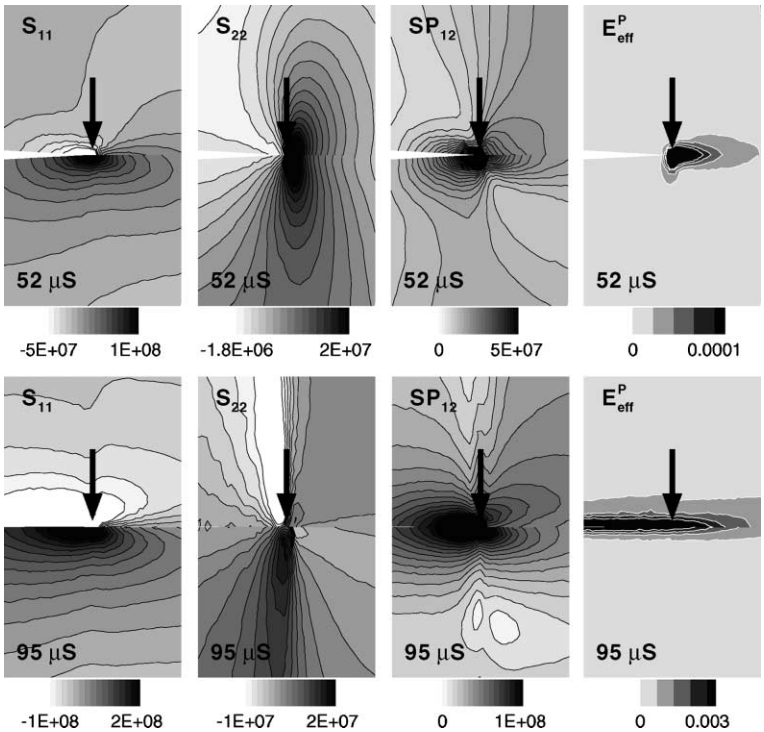

Fig. 13. Contours of S_{11}, S_{22}, SP_{12} and E^{p}_{eff} for the case of 10 m/s impact velocity at onset of crack extension (top) and at steady state of maximum crack speed (bottom).

5.2.4. Features of intersonic crack propagation

The crack tip field changes in the intersonic regime. Figs. 14 and 15 show crack tip parameters for impact velocities of 30 and 40 m/s at which the crack propagates at intersonic speed. In both cases, the crack tip normal traction is compressive at the onset of crack extension. The release wave generated from the left boundary has not reached the crack tip, as can be inferred from the figures. The tangential traction is oppositely directed while the shear stress is continuous across the interface around the tip. Interface elements fail predominantly under mode II loading. As the crack speed increases and attains steady state, the release pulse catches up and the crack tip develops tensile normal traction, though small in magnitude. The phenomena increases the mixed-mode loading seen by the reduction in the continuity of shear stress across the interface. The crack propagates predominantly in shear, mode II. This shows that though the crack tip loading is mixed-mode, the steady-state intersonic crack propagation takes place under predominantly mode II loading. The plastic region remains small and limited to the crack front and its wake. Most importantly, a shock wave resulting from the crack propagating at a speed higher than shear and surface waves, are seen emanating from the crack tip at 49 and 43 μs for the 30 and 40 m/s impact velocity, respectively. The shock waves are shown more clearly in Fig. 16 for the two impact velocities. In the figure, the shock wave is marked by white dashed lines.

When the impact velocity is 30 m/s, the onset of crack extension occurs at 32.4 μs predominantly in shear. At this instant, the release wave, in the lower half plate, is reaching the crack front and the upper half plate, near the crack tip, is under compression. The crack tip and its surrounding remain under compression. The crack accelerates and attains maximum speed at steady state under primarily mode II loading. As the release wave, in the lower half plate, catches up, the crack tip

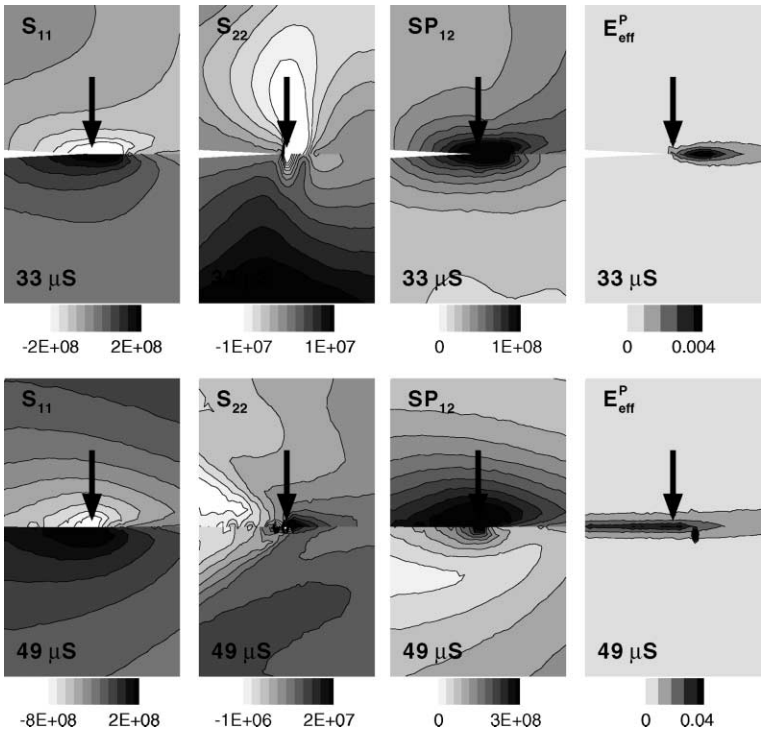

Fig. 14. Contours of S_{11}, S_{22}, SP_{12} and E^{p}_{eff} for the case of 30 m/s impact velocity at onset of crack extension (top) and at steady state of maximum crack speed (bottom).

normal loading changes to tensile. This change in mixed-mode loading coincides with oscillations in crack speed as can be seen in Fig. 12. However, these oscillations are small and the propagation speed can be assumed to be steady at its maximum value. A single shock wave, manifested as a stress discontinuity, develops behind the propagating crack tip in the upper half. This is evidently noticeable in the normal stress contours at 49 μs and also noticeable in the tangential and shear stress contours. Fig. 16 shows that the line of discontinuity emanates from the crack tip. The shock wave trails the crack tip preserving its magnitude. The inclination of the discontinuity with respect to a vertical line remains constant during steady-state propagation as expected. The prediction of a single shock wave is in contrast to our earlier analyses, Dwivedi and Espinosa (2001), in which two discontinuity lines, one emanating from the crack tip and another behind it, were predicted for a 125 mm wide plate and an interface with a shear strength of 300 MPa. *This difference suggests that formation of shock waves and their features are strongly dependent on the interface properties and plate dimensions*. It should be noted that formation of two shock waves were also experimentally observed (Coker and Rosakis, 2001), as a function of impact velocity.

A similar phenomenon occurs when the impact velocity is 40 m/s. The release wave in the upper half plate entraps the compressive stress field present at the crack front. The interaction of this release wave with the compressive field creates an intense shear stress field ahead of the crack tip. A stress discontinuity develops, as seen in Figs. 15 and 16, when the crack propagates intersonically. The inclination of the discontinuity line, from the vertical line, is slightly larger than the inclination for the 30 m/s impact velocity.

5.2.5. Nature of mode mixity with increased impact velocity

The normal and tangential traction histories at the center of the interface elements along the crack

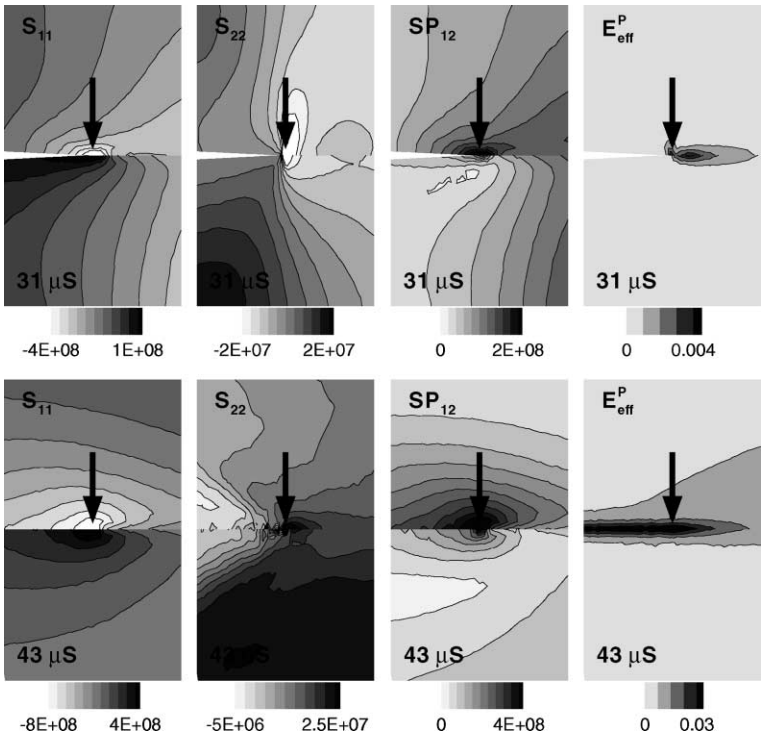

Fig. 15. Contours of S_{11}, S_{22}, SP_{12} and E^{p}_{eff} for the case of 40 m/s impact velocity at onset of crack extension (top) and at steady state of maximum crack speed (bottom).

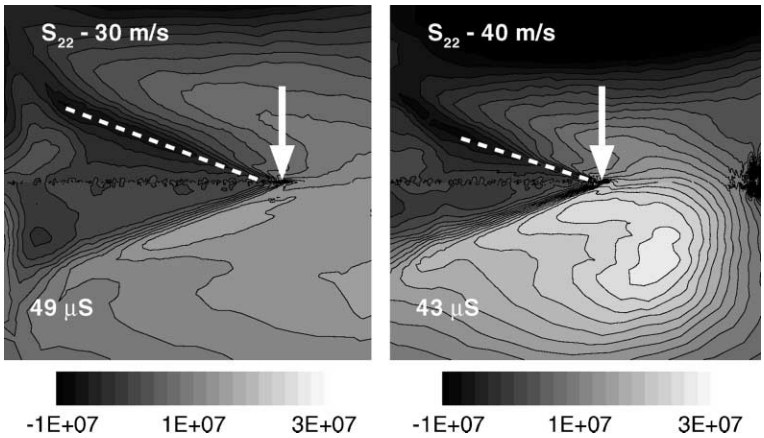

Fig. 16. Shock wave trailing behind the crack tip propagating at intersonic speed for the 30 m/s (left) and 40 m/s (right) impact velocities.

path are shown in Fig. 17, for impact velocity of 5 m/s, and in Fig. 18, for impact velocities of 30 m/s (left) and 40 m/s (right). Starting from the first element at the pre-notch tip (plotted in black), the tractions are plotted at an interval of 20 interface elements, i.e., element numbers 1, 21, 41, etc. At 5 m/s impact velocity, the crack extension occurs under mixed-mode loading. This is seen by the

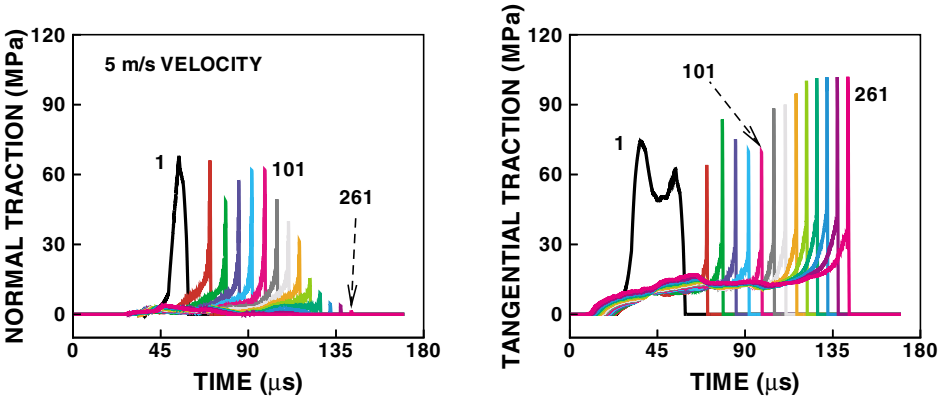

Fig. 17. Crack tip loading history along the crack propagation path, for the case of 5 m/s impact velocity, plotted at an interval of 20 interface elements. Stress peaks in normal and tangential tractions, from left to right, correspond to sequence of interface elements ahead of the pre-crack tip.

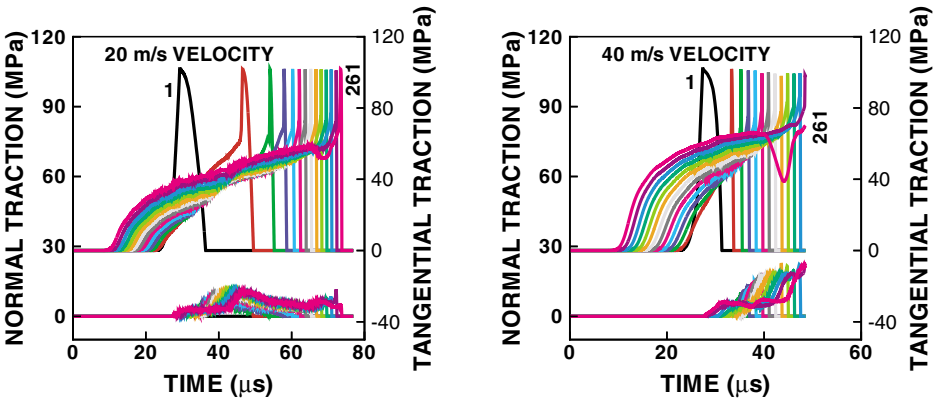

Fig. 18. Crack tip loading history along the crack propagation path, for the case of 30 m/s (left) and 40 m/s (right) impact velocities, plotted at an interval of 20 interface elements. Top curves correspond to the tangential component of the traction vector, while the bottom curves correspond to the normal traction component. Stress peaks in tangential traction, from left to right, correspond to sequence of interface elements ahead of the pre-crack tip.

comparable magnitude of normal and tangential tractions at element 1. The normal traction remains predominant and crack propagates under mixed mode till the failure of element number 91. Subsequently, the normal traction starts decreasing while the tangential traction increases from element number 121 onwards. This phenomenon is found to occur as the crack tip velocity approaches the shear wave speed C_s (see Fig. 12). This change in the loading mode from mixed to predominantly mode II is associated to the increase in crack speed, as discussed earlier for the case of 10 m/s impact velocity. At an impact velocity of 30 m/s, which leads to intersonic crack propagation, the normal traction at the onset of crack extension is quite small when compared to the tangential traction (see Fig. 18, left and bottom). The interface is loaded predominantly in shear during failure. As the crack propagates, the normal traction increases due to the arrival of a tensile pulse, but the magnitude remains below 20 MPa. Similar phenomena take place at an impact velocity of 40 m/s. The normal traction developed during propagation is larger when compared to the 30 m/s case

due to the increase in pulse amplitude. Nevertheless, the intersonic crack propagation at both velocities occurs under predominantly mode II loading. In the sub-sonic regime, crack propagation also takes place under mixed-mode loading but with equal contribution of modes. An increase in the imparted energy increases mode II loading at the crack tip and, consequently, increases the crack speed. Similar findings were reported by Geubelle and Kubair (2001) for the case of shear cracks in homogeneous media.

5.2.6. Contact behind the crack tip

As previously mentioned, analyses predict contact behind intersonically propagating crack tips. Figs. 19 and 20 show contours of longitudinal stress at the onset of crack extension and at the instant of maximum crack speed, for the cases of 5 and 40 m/s impact velocities, respectively. When the impact velocity is 5 m/s, the crack propagates at sub-sonic speed and opens. The crack front remains open throughout the event due to tensile normal tractions. By contrast, at 40 m/s, compressive normal tractions are observed, behind the intersonically propagating crack tip, and a well developed large contact zone is observed (see Fig. 20). At this impact velocity, the entire crack wake remains closed as if the plate would have never failed.

5.2.7. Effect of friction on intersonic crack propagation

All the above analyses results are for the case of frictionless crack surfaces. Further analyses were carried out, for the impact velocities of 30 and 40 m/s, when the friction coefficient is 0.5, 1, 5 and 10. The crack speed history for the five values of friction coefficients are shown in Fig. 21; for 30 m/s (left) and 40 m/s (right) impact velocities. The figure shows that the crack extension time and

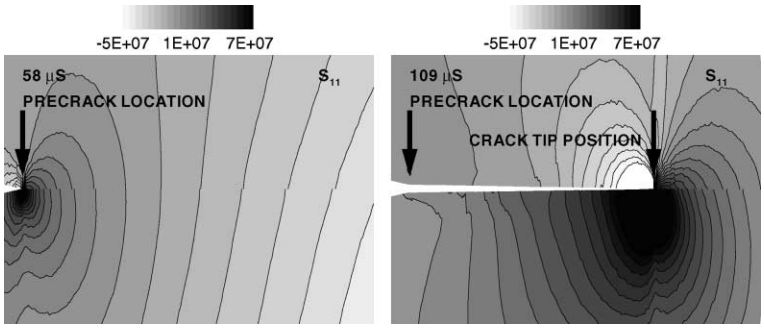

Fig. 19. Sub-sonic crack propagation and open crack front for the case of 5 m/s impact velocity.

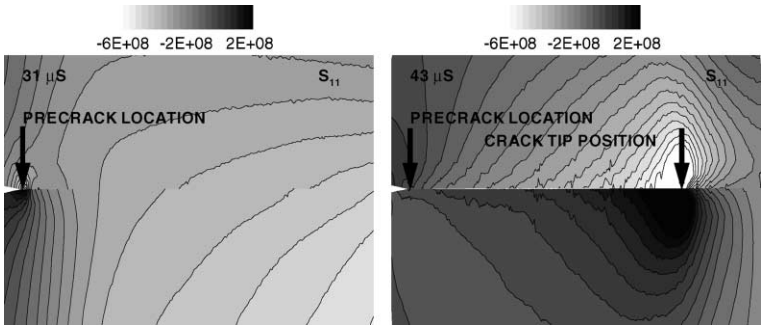

Fig. 20. Intersonic crack propagation and close crack front for the case of 40 m/s impact velocity.

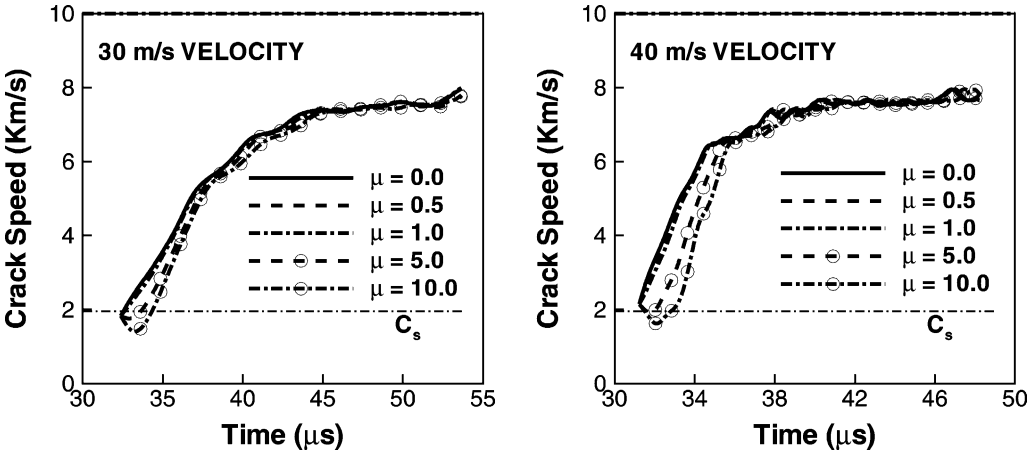

Fig. 21. Effect of friction along the crack front on the intersonic crack speed for 30 m/s (left) and 40 m/s (right) impact velocities.

steady-state speed remains unchanged with the increase in friction. A friction coefficient of up to 1 does not have any discernible effect on the crack propagation history. However after the onset of extension, when the friction coefficient is larger, say equal to 5, the crack speed first reduces and then increases. The reduction is larger as the friction coefficient is increased from 5 to 10. However, friction does not have an appreciable effect on the maximum crack speed at steady state. A more remarkable effect due to the increase in friction coefficient is observed in the stress field behind the crack tip.

Figs. 22 and 23 compare the shock wave orientation emanating from the crack tip at the instant of steady-state crack speed. Remarkably, the increase in friction coefficient spreads the region of compressive stress over a larger area in front of the crack tip. This smearing effect is also associated with the increase in compressive stress and the increase in inclination of the discontinuity line with respect to the vertical line.

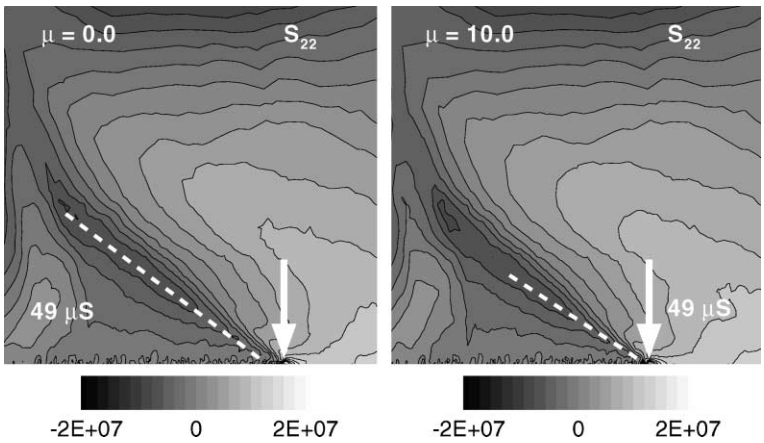

Fig. 22. Shock wave for frictionless crack surfaces (left) and with a friction coefficient of 10 (right). Impact velocity is 30 m/s. Arrows indicate crack tip position.

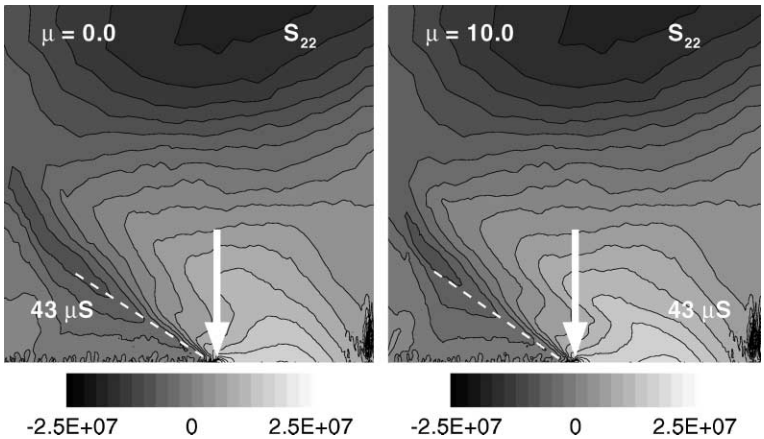

Fig. 23. Shock wave for frictionless crack surfaces (left) and with a friction coefficient of 10 (right). Impact velocity is 40 m/s. Arrows indicate crack tip position.

5.2.8. Path independent integral J' vs. impact velocity

The path independent integral J' history calculated for various contours are shown in Fig. 24 for the impact velocities of 10 m/s (left) and 40 m/s (right). All values of J' here reported are for the case of frictionless crack surfaces. It is found that J' is basically path independent as long as release waves, from the plate boundaries, do not enter the domain of integration used to compute J'. In the case of sub-sonic crack propagation this is the case up to about 50 μs. For intersonic crack propagation, impact velocity of 40 m/s, J' is path independent only for contours close to the crack tip. Note that J' value at contours 1 and 2 (refer to Fig. 11) are the same within the desired tolerance. However, the value of J' increases with distance from the crack tip, as seen for contours 3–5. This occurs because the contours begin to capture effects from release waves emanating from the plate boundaries. It can be inferred that J' can serve as a characterizing parameters for dynamic crack propagation if computed close to the crack tip field. J' for contours 1 and 2 starts increasing from

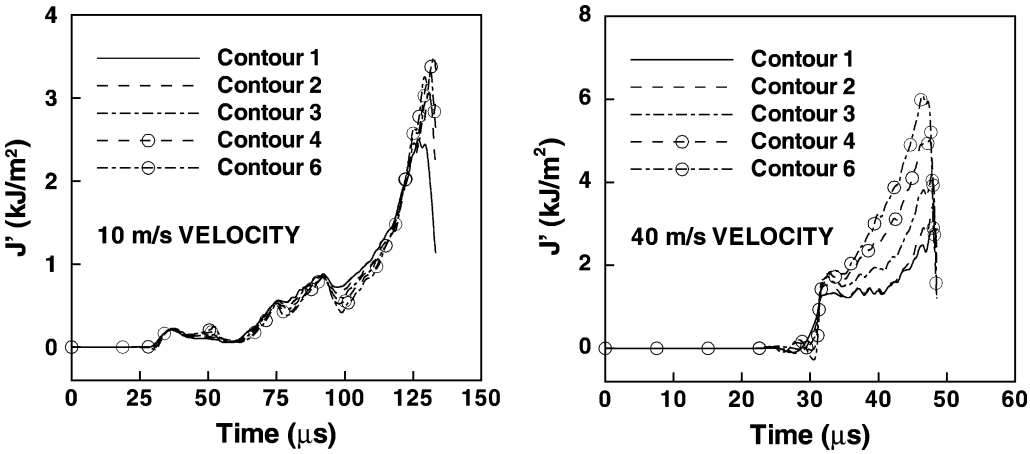

Fig. 24. J' value at different contours for impact velocities of 10 m/s (left) and 40 m/s (right).

27.4 μs. The average value for the two contours at the onset of crack extension, at 31.2 μs, is 1250 J/m^2, which compares well to the G_{Ic} of 300 J/m^2 and G_{IIc} of 900 J/m^2. After crack extension, J' increases slightly and attains the value of 1400 J/m^2 at 40.5 μs. This represents an increase of 12% with respect to the value at onset. However, from 40.5 μs onwards, J' starts increasing at a much higher rate. This increase can be attributed to the interaction of the crack tip stress field with release wave stress fields. As mentioned earlier, the steady-state intersonic crack speed is close to the material longitudinal wave speed. This eventually leads to interaction of the crack tip stress field with release stress waves originating at the boundaries of the finite size composite plate. In other words, the transient reflected stress field makes the calculation contour dependent. This is reflected in the pronounced increase in the value of J' after 40.5 μs. Even at the last three contours, J' remains approximately constant for a while and then starts increasing. The increase in J' is observed until approximately 47.5 μs and then it starts to drop. This reduction occurs due to the interaction of the crack tip stress state with the bonded zone at the end of the interface line and must not be confused with a feature of intersonic crack propagation. The approximately constant value of J', computed during steady-state crack propagation and before boundary effects enter the domain delineated by the outer contour, indicates that this parameter can be used as a characteristic material property corresponding to intersonic crack propagation.

6. Conclusions

The simulations presented in this article show that the proposed model adequately predicts the phenomenon of dynamic crack propagation in bimaterials and fiber reinforced composites. The crack speed and the path independent integral J' obtained from the present analyses agree well with the data reported in the literature.

The present numerical study confirms the phenomenon of intersonic crack propagation in fiber reinforced composite materials, for which limited experimental data exist in the literature. Due to inherent anisotropy, cracks propagate in fiber composite materials under mixed-mode loading conditions. However, the associated phenomenon depends mainly on the imparted impact energy. At low impact velocities, below 20 m/s, the crack propagates at sub-sonic speed, i.e., below the shear wave speed of the material. Mode I loading of the crack tip is comparable to mode II loading in this regime. As a result, the crack front remains open and no line of discontinuity or shock wave emanates from the propagating crack tip.

At higher impact velocities, 20 m/s or more, steady-state intersonic crack propagation is predicted by the present simulations. The maximum crack speed at steady state, for 20, 30 and 40 m/s impact velocities, is found to be as high as 3.9 times the shear wave speed and 83% of the longitudinal wave speed of the material. Mode II loading of the crack speed becomes more and more predominant as the crack speed increases in the intersonic regime. A discontinuous line and resulting large contact zone behind the intersonically propagating crack are predicted by these analyses. These findings are in total agreement with the experimental observations of Coker and Rosakis (1998, 2001) even when our simulations were not based on the same exact plate dimension and composite properties. Our computational results are also consistent with the analytical predictions reported in Huang et al. (1999). These authors found that in the steady-state regime, an asymptotic elastic field gives a finite and non-vanishing energy flux into the crack tip only when the crack velocity is equal to $\sqrt{(C_{11}C_{22} - C_{12}C_{12})/C_{66}(C_{12}C_{22})}C_s$. In fact, our simulations show that above a given impact velocity threshold, the crack accelerates toward this critical velocity until a steady state is reached. How fast this state is attained is a function of impact velocity, i.e., the amount of energy delivered to the crack tip, when a constant cohesive energy is assumed. Moreover, the calculations reveal that during the unsteady states, other crack tip velocities are possible with a non-vanishing value of J' in agreement with the analyses reported by Broberg (1999). A similar computational finding was reported by Needleman (1999) for the

particular case of shear cracks in homogeneous materials having a weak plane (see also Burridge et al., 1979).

The simulations show that the contour integral J' is constant for near field contours. The pre-notch tip stores energy slightly in excess of the specified critical strain energy release rate G_{IIc}. However, it remains constant during the steady-state crack propagation phase. This is in contrast to available literature results based on singular models of fracture in which the strain energy release rate reduces to zero as the crack speed increases in the intersonic regime. The analyses also show that J' can serve as a parameter for establishing conditions for dynamic crack propagation in materials subjected to stress wave loading. Further studies are needed to elucidate the effect of the friction coefficient on J'. Likewise, numerical results sensitivity to plate and mesh dimensions needs further investigation.

The simulations also show that very high friction in the crack surfaces has an effect on crack propagation. Increased friction reduces the crack speed after initiation, however the maximum crack speed at steady state remains unchanged. Increased friction also smears the shock wave and increases its inclination with respect to a vertical direction. Our simulations indicate that the effect of release waves from boundaries and the effect of interface strength on shock wave formation are important and need to be experimentally and computationally studied in greater detail.

The computational results also highlight that the stress wave history plays an important role on the crack propagation event. It was observed that beyond a certain time, the propagating crack tip stress field interacts with release stress waves generated at the plate right boundary. The effect thereafter is devastating with a number of crack nuclei originating simultaneously ahead of the crack tip. The calculations were ended beyond this point in order to study the steady-state regime of the propagating crack in isolation. This is an important observation from the view point of carrying out and interpreting experiments. In order to eliminate such interaction, it becomes necessary to select sample dimensions and loading conditions appropriately.

Lastly, it should be emphasized that the computational methodology here presented can be applied to a variety of technological problems of interest in which contact *and* friction behind the crack tip needs to be accounted for. Applications in which such tool is particularly useful is not restricted to the analysis of novel heterogeneous materials but also to homogeneous materials. For instance, in earthquake predictions involving dynamic shear cracks propagating in the Earth's crust.

Acknowledgements

This research was supported by the National Science Foundation through Career Award no. CMS-9624364, the Office of Naval Research YIP through Award no. N00014-97-1-0550, the Army Research Office through ARO-MURI Award no. DAAH04-96-1-0331 and the Air Force Office of Scientific Research through Award no. F49620-98-1-0039. The ONR support in the form of supercomputer account to carry out analyses is acknowledged. A special thank is due to Ares Rosakis and Phillipe Geubelle for providing key scientific comments during the preparation of the manuscript. The assistance from Mr. Sungsoo Lee in the editing of the article is greatly appreciated.

References

Aboudi, J., 1989. Micromechanical analysis of composites by the method of cells. Applied Mechanics Reviews 42, 193–221.

Atluri, S.N., 1982. Path-independent integrals in finite elasticity and inelasticity, with body forces, inertia, and arbitrary crack-face conditions. Engineering Fracture Mechanics 16 (3), 341–364.

Broberg, K.B., 1999. Intersonic crack propagation in an orthotropic material. International Journal of Fracture 99, 1.

Burridge, R., Conn, G., Freund, L.B., 1979. The stability of a rapid mode II shear crack with finite cohesive traction. Journal of Geophysics Research 85, 2210–2222.

Camacho, G.T., Ortiz, M., 1996. Computational modeling of impact damage in brittle materials. International Journal of Solids and Structures 33 (20-22), 2899–2938.

Carpenter, W.C., Read, D.T., Dodds Jr., R.H., 1986. Comparison of several path independent integrals including

plasticity effects. International Journal of Fracture 31, 303–323.

Chen, J.K., Allahdadi, F.A., Sun, C.T., 1997. A quadratic yield function for fiber-reinforced composites. Journal of Composite Materials 31 (8), 788–811.

Coker, D., Rosakis, A.J., 1998. Experimental observations of intersonic crack growth in asymmetrically loaded unidirectional composite plates, GALCIT-SM Report 98-16. CALTECH, Pasadena, CA, 1998.

Coker, D., Rosakis, A.J., 2001. Experimental observations of intersonic crack growth in asymmetrically loaded unidirectional composite plates. Philosophical Magazine A 81, 571–595.

Dwivedi, S.K., Espinosa, H.D., 2001. Modeling intersonic crack propagation in fiber reinforced composites with contact/cohesive laws. In: Waas, A.M., Whitcomb, J.D. (Eds.), Damage Initiation and Prediction in Composites, Sandwich Structures and Thermal Barrier Coatings. 2001 ASME International Mechanical Engineering Congress and Exposition, November 11–16, New York, NY, vol. 66, pp. 121–153.

Espinosa, H.D., Lu, H.-C., Dwivedi, S., Zavattieri, P.D., 1997. A finite deformation anisotropic plasticity model for fiber reinforced composites. In: Proceedings of 12th Annual Technical Conference of the American Society for Composites, Dearborn, MI, pp. 429–441.

Espinosa, H.D., Zavattieri, P.D., Dwivedi, S., 1998a. A finite deformation continuum/discrete model for the description of fragmentation and damage in brittle materials. Journal of Mechanics and Physics of Solids 46 (10), 1909–1942.

Espinosa, H.D., Zavattieri, P.D., Emore, G.L., 1998b. Adaptive FEM computation of geometric and material nonlinearities with application to brittle failure. Mechanics of Materials 29, 275–305.

Espinosa, H.D., Dwivedi, S., Lu, H-C., 1999. Modeling impact induced delamination of woven fiber reinforced composites with contact/cohesive laws. Computer Methods in Applied Mechanics and Engineering 183 (3–4), 259–290.

Espinosa, H.D., Lu, H.-C., Zavattieri, P.D., Dwivedi, S., 2001. A 3-D finite deformation anisotropic visco-plasticity model for fiber composites. Journal of Composite Materials 35 (5), 369–410.

Espinosa, H.D., Zavattieri, P.D., 2002a. A grain level model for the study of failure initiation and evolution in polycrystalline brittle materials, Part I: Theory and numerical implementation, this volume.

Espinosa, H.D., Zavattieri, P.D., 2002b. A grain level model for the study of failure initiation and evolution in polycrystalline brittle materials, Part II: Numerical examples, this volume.

Geubelle, P., Baylor, J., 1998. Impact-induced delamination of composites: A 2D simulation. Composites B 29B, 589–602.

Geubelle, P.H., Kubair, D., 2001. Intersonic crack propagation in homogeneous media under shear-dominated loading: numerical analysis. Journal of Mechanics and Physics of Solids 49 (3), 571–587.

Huang, Y., Wang, W., Liu, C., Rosakis, A.J., 1999. Analysis of intersonic crack growth in unidirectional fiber-reinforced composites. Journal of the Mechanics and Physics of Solids 47, 1893–1916.

Hwang, C., Geubelle, P., 2000. A spectral scheme to simulate dynamic fracture problems in composites. Computer Modeling in Engineering and Sciences 1 (4), 45–56.

Kavaturu, M., Shukla, A., 1998. Dynamic fracture criteria for crack growth along bimaterial interfaces. Journal of Applied Mechanics, Trans. ASME 65, 293–299.

Kumar, P., Kishore, N.N., 1998. Initiation and propagation toughness of delamination crack under an impact load. Journal of the Mechanics and Physics of Solids 46 (10), 1773–1787.

Lambros, J., Rosakis, A.J., 1995a. Shear dominated transonic interfacial crack growth in a bimaterial—I. Experimental observations. Journal of the Mechanics and Physics of Solids 43 (2), 169–188.

Lambros, J., Rosakis, A.J., 1995b. Development of a dynamic decohesion criterion for subsonic fracture of the interface between two dissimilar materials. Proceedings of the Royal Society of London A 451, 711–736.

Lambros, J., Rosakis, A.J., 1995c. Dynamic decohesion of bimaterials: Experimental observations and failure criteria. International Journal of Solids and Structures 32 (17/18), 2677–2702.

Lambros, J., Rosakis, A.J., 1997. Dynamic crack initiation and growth in thick unidirectional graphite/epoxy plates. Composites Science and Technology 57, 55–65.

Lee, S-W.R., Sun, C.T., 1992. A quasi-static penetration model for composite laminates. Journal of Composite Materials 27, 251–271.

Lee, S-W.R., Sun, C.T., 1993. Dynamic penetration of graphite/epoxy laminates impacted by a blunt-ended projectile. Composites Science and Technology 49, 369–380.

Li, F.Z., Shih, C.F., Needleman, A., 1985. A comparison of methods for calculating energy release rates. Engineering Fracture Mechanics 21 (2), 405–421.

Liu, C., Lambros, J., Rosakis, A.J., 1993. Highly transient elastodynamic crack growth in a bimaterial interface: Higher order asymptotic analysis and optical experiments. Journal of the Mechanics and Physics of Solids 41 (12), 1887–1954.

Liu, C., Huang, Y., Rosakis, A.J., 1995. Shear dominated transonic interfacial crack growth in a bimaterial—II. Asymptotic fields and favorable velocity regimes. Journal of the Mechanics and Physics of Solids 43 (2), 189–206.

Lo, C.Y., Nakamura, T., Kushner, A.S., 1993. Dynamic failure analysis along interfaces in composite materials. Advanced Computational Methods for Material Modeling, AMD-vol. 180/PVP-268. ASME, pp. 115–124.

Moran, B., Shih, C.F., 1987. Crack tip and associated domain integrals from momentum and energy balance. Engineering Fracture Mechanics 27 (6), 615–642.

Nakamura, T., Shih, C.F., Freund, L.B., 1985. Computational methods based on an energy integral in dynamic

fracture. International Journal of Fracture 27, 229–243.

Nakamura, T., Kushner, A., Lo, C.Y., 1995. Interlaminar dynamic crack propagation. International Journal of Solids and Structures 32 (17/18), 2657–2675.

Needleman, A., 1999. An analysis of intersonic crack growth under shear loading. Journal of Applied Mechanics 66, 847–857.

Needleman, A., Rosakis, A.J., 1999. The effect of bond strength and loading rate on the attainment of intersonic crack growth in interfaces. Journal of Mechanics and Physics of Solids 47, 2411–2449.

Nishioka, T., 1994. The state of the art in computational dynamic fracture mechanics. JSME International Journal—Series A 37 (4), 313–333.

O'Donoghue, P.E., Anderson Jr., C.E., Friesenhahn, G.J., Parr, C.H., 1992. A constitutive formulation for anisotropic materials suitable for wave-propagation computer-programs. Journal of Composite Materials 26 (13), 1860–1884.

Paley, M., Aboudi, J., 1992. Micromechanical analysis of composites by the generalized cells model. Mechanics of Materials 14, 127–139.

Pandey, R.K., Sun, C.T., 1996. Calculating strain energy release rate in cracked orthotropic beams. Journal of Thermoplastic Composite Materials 9, 381–395.

Ricci, V., Shukla, A., Singh, R.P., 1997. Evaluation of fracture mechanics parameters in bimaterial systems using strain gages. Engineering Fracture Mechanics 58 (4), 273–283.

Rice, J.R., Suo, Z., Wang, J.-S., 1990. Mechanics and thermodynamics of brittle interfacial failure in bimaterial systems. Metal–ceramic interfaces. Acta-Scripta Metallurgica Proceedings Series 4, 269–294.

Rosakis, A.J., Lee, Y.J., Lambros, J., 1991. Dynamic crack growth in bimaterial interface. Experiments in micromechanics of failure resistant materials, AMD-vol. 130. ASME, pp. 17–23.

Rosakis, A.J., Samudrala, O., Coker, D., 1999. Cracks faster than shear wave speed. Science 284, 1337–1340.

Shih, C.F., Asaro, R.J., 1990. Elastic–plastic and asymptotic fields of interface cracks. International Journal of Fracture 42, 101–116.

Siegmund, T., Fleck, N.A., Needleman, A., 1997. Dynamic crack growth across an interface. International Journal of Fracture 85, 381–402.

Singh, R.P., Shukla, A., 1996. Subsonic and intersonic crack growth along a bimaterial interface. Journal of Applied Mechanics. Trans. ASME 63, 919–924.

Singh, R.P., Lambros, J., Shukla, A., Rosakis, A.J., 1997a. Investigation of the mechanics of intersonic crack propagation along a bimaterial interface using coherent gradient sensing and photoelasticity. Proceedings of the Royal Society of London A 453, 2649–2667.

Singh, R.P., Kavaturu, M., Shukla, A., 1997b. Initiation, propagation and arrest of an interface crack subjected to controlled stress wave loading. International Journal of Fracture 83, 291–304.

Stout, M.G., Liu, C., Ellis, R.W., Haberman, K.S., Bennet, J.G., Williams, Addesio, F.L., Rosakis, A.J., 1998. Mechanics analysis and simulation of a graphite/epoxy composite plate. In: Allison (Ed.), Experimental Mechanics, pp. 187–192.

Sun, C., Chen, J.L., 1989. A simple flow rule for characterizing the nonlinear behavior of fiber composites. Journal of Composite Materials 23, 1009–1020.

Sun, C.T., Wu, X.X., 1996. On the J-integral in periodically layered composites. International Journal of Fracture 78, 89–100.

Sun, C.T., Qian, W., 1997. The use of finite extension strain energy release rates in fracture of interfacial cracks. International Journal of Solids and Structures 34 (20), 2595–2609.

Tippur, H.V., Rosakis, A.J., 1991. Quasi-static and dynamic crack growth along bimaterial interfaces: A note on crack-tip field measurements using coherent gradient sensing. Proceeding of the Society for Experimental Mechanics 48, 243–251.

Tippur, H.V., Krishnaswamy, S., Rosakis, A.J., 1991. A coherent gradient sensor for crack tip deformation measurements: analysis and experimental results. International Journal of Fracture 48, 193–204.

Varias, A.G., O'Dowd, N.P., McHugh, P.E., Shih, C.F., 1990a. Computational modeling of interface failure. In: Kinzel, G.L., Rhode, S.M. (Eds.), Proceedings of the 1990 ASME International Computers in Engineering Conference, vol. 2, pp. 671–689.

Varias, A.G., O'Dowd, N.P., Asaro, R.J., Shih, C.F., 1990b. Failure of bimaterial interfaces. Materials Science and Engineering A 126, 65–93.

Voyiadjis, G.Z., Thiagarajan, G., 1995. An anisotropic yield surface model for directionally reinforced metal matrix composites. International Journal of Plasticity 11, 867–894.

Voyiadjis, G.Z., Thiagarajan, G., 1996. A cyclic anisotropic-plasticity model for metal matrix composites. International Journal of Plasticity 12 (1), 69–91.

Weeks, C.A., Sun, C.T., 1996. Nonlinear rate dependent response of thick-section composite laminates. High Strain Rate Effects on Polymer, Metal and Ceramic Matrix Composites and other Advanced Materials. ASME AD-vol. 48, pp. 81–95.

Weeks, C.A., Sun, C.T., 1998. Modeling non-linear rate-dependent behavior in fiber reinforced composites. Composites Science and Technology 58 (3-4), 603–611.

Wu, K-C., 1991. Explicit crack-tip fields of an extending interface crack in an anisotropic bimaterial. International Journal of Solids and Structures 27 (4), 455–466.

Xu, X.-P., Needleman, A., 1995. Numerical simulations of dynamic interfacial crack growth allowing for crack growth away from the bond line. International Journal of Fracture 74, 253–275.

Xu, X.-P., Needleman, A., 1996. Numerical simulations of dynamic crack growth along an interface. International Journal of Fracture 74, 289–324.

Xu, X.-P., 1996. Dynamic fracture via molecular dynamics and cohesive finite element methods. Advances in Failure Mechanisms in Brittle Materials, MD-vol. 75/AMD-vol. 219. ASME, pp. 99–107.

Yang, W., Suo, Z., Shih, C.F., 1991. Mechanics of dynamic debonding. Proceedings of the Royal Society of London A 433, 679–697.

Zheng, S., Sun, C.T., 1995. A double-plate finite-element model for the impact-induced delamination problem. Composites Science and Technology 53, 111–118.